Department of Physics and Astronomy

University of Heidelberg

Bachelor Thesis in Physics

submitted by

Michael Rautenberg

born in Herdecke (Germany)

2018

Diagnosing Quantum Chaos in a Spinor Bose Einstein Condensate

This Bachelor Thesis has been carried out by Michael Rautenberg at the
Kirchhoff Institut für Physik in Heidelberg
under the supervision of
Prof. Thomas Gasenzer and Dr. Martin Gärttner

Zusammenfassung

In der vorliegenden Arbeit soll die Verbindung zwischen Chaos in klassischen und quantenmechanischen Systemen theoretisch und numerisch für ein Spin 1 Spinor Bose Einstein Kondensat untersucht werden. Genauer gesagt, werden wir versuchen, Größen in der quantenmechanischen Theorie zu finden, die zu entscheiden erlauben, ob die Theorie im klassischen Grenzfall reguläres oder chaotisches Verhalten aufweist. Ein Hauptaugenmerk wird dabei auf nicht zeitgeordneten Korrelationsfunktionen (OTOCs) liegen, da diese einen wohldefinierten klassischen Grenzwert haben, in dem sie einem bestimmen Lyapunov Exponenten entsprechen, einem Indikator für klassisches Chaos. Um zu sehen, ob OTOCs als Indikatoren für Quantenchaos dienen können, werden wir zuerst die klassische mean field Theorie konstruieren und mit etablierten Techniken wie Poincaré Schnitten und Lyapunov Exponenten analysieren, für welche Parameter und Anfangszustände sie chaotisches Verhalten zeigt. Dann werden wir die quantenmechanische Theorie simulieren um zu entscheiden, ob OTOCs oder andere Methoden, wie die Analyse der Statistik der Eigenwertabstände des Hamiltonian, ähnliche chaotische Regionen reproduzieren können.

Abstract

In this thesis the connection between chaos in classical and quantum mechanical systems will be examined theoretically and numerically for a spin 1 spinor Bose Einstein condensate. More precisely, we will try to find quantities in the quantum theory that allow to decide whether the classical limit of that theory shows regular or chaotic behaviour. One main focus will be on out-of-time-ordered correlators (OTOCs) as they have a well-defined classical limit where they can be associated with a certain (classical) Lyapunov exponent, a quantity known to indicate classical chaos. To see whether OTOCs can be used as a proxy for quantum chaos, we will first construct the classical mean field theory and analyse for what parameters and initial states it shows chaotic behaviour using well established techniques such as Poincaré sections and Lyapunov exponents. Then, we will simulate the quantum theory to decide, whether OTOCs or other techniques such as the analysis of the level spacing statistics of the Hamiltonian can reproduce similar chaotic regions.

Contents

1 Introduction

1.1 Motivation

Quantum chaos, i.e. the generalization of the well-established concepts concerning classical chaos to quantum systems, is subject to current research [1, 2, 3]. This is because, although classical chaos has been thoroughly studied and is considered to be a well understood field [4], it is conceptually not clear, what chaos means in quantum mechanics. A minimal definition of quantum chaos would be to call a quantum mechanical system chaotic if its corresponding classical limit is classically chaotic. In this setting, the aim is to find tools or schemes that can serve as a proxy for quantum chaos, i.e. quantities of the quantum theory that have well-defined classical limits which allow to decide whether the classical theory is chaotic. Finding such quantities turns out not to be easy, one reason being that naïve generalizations of indicators for classical chaos often fail, as will be discussed in section 2.1. But there are also promising ideas, such as to take the concept of exponentially diverging classical trajectories measured by the Lyapunov exponent and going through a quantization procedure eventually arriving at so-called "out-of-time-order correlators" (OTOCs) [5]. These correlators have a well-defined classical limit by construction, but are not easy to measure experimentally: Loosely speaking, OTOCs compare the action of two operators acting on a given state at different times and in different successions, i.e. in order to measure them one has to be able to evolve states forward and backwards in time[1], see section 2.1. Very precise control of the quantum system is needed to realize this "time machine" explaining why this work focuses on spinor dynamics in a Bose Einstein condensate. In this system we can realize the time reversal schemes necessary to measure OTOCs by changing all parameters of our Hamiltonian to their exact negative. The evolution under this negative Hamiltonian amounts to an evolution backwards in time as is shown in the same section. Although this work is done having in mind the experimental realization, I will only concern myself with the theory and its simulations. But even simulating OTOCs on classical

[1]There are also other ideas for experimental implementations of OTOCs, see e.g. [6], but they are not easier to realize.

computers, just as quantum many body systems in general, is a hard task due to the known exponential dependence of the computational effort on the number of simulated particles[2].

Despite these obstacles, quantum chaos is a very interesting field of research as knowledge about it would allow us to gain a better understanding of seemingly unrelated topics such as the dynamics of black holes and the information paradox [7]. To see that these topics are indeed related, consider the following (adapted from [7]): The information paradox asks how information about objects that fell into a black hole can be both trapped inside the event horizon and at the same time liberated by Hawking radiation. As black holes are thermal objects, this question is strongly related to how information dynamics lead to thermalisation. To quantify this process of information scrambling in quantum systems we can e.g. rely on OTOCs.

1.2 Objectives

Although quantum chaos has already been studied in numerous publications, I will focus on quantum chaos and its classical limit in spin 1 spinor systems which - in this form - has not been done yet. This system is particularly suited for these purposes as it is the lowest dimensional spinor system where one can possibly observe chaotic behaviour in the corresponding classical system (in the non driven case): To observe chaotic behaviour in a collective spin system composed of spin 1/2 particles, one has to drive it periodically, breaking energy conservation symmetry, see e.g. [2]. If one wants to see chaotic behaviour without modifying the original Hamiltonian (as it will be done in this work) one has to go to a higher dimensional system, e.g. a spinor BEC in single mode approximation[3] in $|F = 2\rangle$, see [8]. The impact of the phase space dimension on the possibility of chaos will be discussed in detail in section 3.3. Another reason why the spin 1 spinor BEC is a nice system to study quantum chaos and especially OTOCs is because it

[2]In our case, as we restrict to the fully symmetric Fock space, the Hilbert space dimension only scales quadratically in the number of particles.

[3]If momentum modes can be excited in the BEC, chaotic behaviour is also observable in $|F = 1\rangle$ BECs. This work focuses entirely on the internal spinor dynamics.

offers the possibility to implement time reversal schemes experimentally and thus allows the measurement of OTOCs.

In brief, my objectives can be described as follows: First, I will construct the classical mean field theory corresponding to the quantum mechanical spinor system and determine chaotic areas, i.e. regions in parameter space where the system exhibits classically chaotic behaviour. Then, I will do the "full" quantum simulations and test, whether quantities such as OTOCs, that have been proposed as a proxy for quantum chaos, can reproduce similar regions where the system is "quantum chaotic".

Outline

In the first part of this thesis some information about the theoretical background of the field is given: Starting with the concept of classical chaos, I will present some attempts to generalize them to quantum systems also introducing OTOCs as they will be one major point of interest in my work. After this general introduction I will focus on the system that will be studied (spin 1 spinor BEC) and why this system was chosen. In this part I will give an overview of the description of a Bose Einstein condensate (BEC) and the formalism I will use to describe the spinor dynamics (namely single mode approximation and Fock basis). The following section of the thesis will present the classical mean field theory corresponding to the quantum system. After showing how the mean field equations can be derived, I will focus on finding chaotic behaviour for a region of parameters (as it will turn out, I have to add an extra term to the Hamiltonian to be able to observe chaos). The main part of this section will be about quantifying classical chaos, focussing on Poincaré maps and Lyapunov exponents.

In section 4, I will examine the quantum system itself doing the full quantum calculations. After having presented the numerical computation schemes, I will focus on visualisation techniques before finally examining the chaoticity: First by analysing statistics of the energy level spacings and then by computing some OTOCs. The last section contains the comparison of the classical and quantum results and in that way can be seen as the conclusion of my thesis as it answers the question to what extend OTOCs can be used to diagnose quantum chaos.

2 Theoretical Background

2.1 Chaos in Classical and Quantum Dynamics

Classical chaos is popularly understood as a system's sensitivity to initial conditions. As phrased by one of the most famous mathematicians working in this field, Edward Lorenz, it reads

> "Chaos: When the present determines the future, but the approximate present does not approximately determine the future."

This notion of high sensitivity to initial conditions is popularly associated with the butterfly effect [9]: In Lorenz's version: A tiny disturbance of the system (here: the flap of a butterfly's wings in Brazil) can lead to a totally different evolution of the system (weather) until it eventually has major effects (tornado in Texas). Bradbury takes this even further [10]: In his story "The sound of thunder" the fact that a butterfly is killed accidentally, results in a completely different evolution of mankind's history.

Returning to a mathematical formulation of chaos, the sensitivity of a dynamical system to initial conditions can be expressed by the Lyapunov exponent (also called Lyapunov characteristic number) [1]. Given a classical trajectory $x(t)$ and some initial conditions x_0, the sensitivity to initial conditions can be expressed as the exponential divergence of initially infinitesimally separated trajectories:

$$\left|\frac{\partial x(t)}{\partial x_0}\right| \propto e^{\lambda t} \tag{1}$$

The Lyapunov exponent λ has to be greater than zero for the system to be chaotic.

But although necessary for chaotic behaviour, a positive Lyapunov exponent is not sufficient: For a dynamical system to be chaotic, it must also be topologically mixing. This means that every given region in phase space has to overlap with every other given region after some finite time.

A final remark on this definition of classical chaos: Although classical chaos has been intensively studied, there is still no universally accepted mathematical definition. However, the two conditions cited above are normally agreed on when talking about classical chaos in physical systems. We now want to generalize the concept of chaos to quantum mechanics. But we run into difficulties when

we try to find an analogue to the butterfly effect because quantum mechanics prohibits the infinitesimal shift of trajectories [11]. One might naïvely think that the overlap of a state $|\psi\rangle$ with another, slightly perturbed state $|\psi'\rangle$ would decay over time, but, due to unitarity of time evolution, this is obviously not the case:

$$\langle\psi'|\, U^\dagger(t)U(t)\,|\psi\rangle = \langle\psi'|\psi\rangle \tag{2}$$

Instead, what can be done to construct an object representing the butterfly effect is the following [1]: Starting with the classical Lyapunov exponent in eq. (1) we replace the derivative by a Poisson bracket (for details, see section 4.5):

$$\frac{\partial x(t)}{\partial x_0} = \{x(t), p_0\}_{\text{Poisson}}\,. \tag{3}$$

Then we can proceed with canonical quantization, i.e. we get the commutator

$$\frac{1}{i\hbar}\,[\hat{x}(t), \hat{p}] \tag{4}$$

where $\hat{x}(t)$ is the position operator in the Heisenberg picture. This expression as an operator might have complex eigenvalues which could lead to cancellations when calculating its expectation value with respect to some density matrix. To avoid these cancellations, it is natural to take its norm squared, i.e.

$$\frac{1}{i\hbar}\,[\hat{x}(t), \hat{p}] \cdot \left(\frac{1}{i\hbar}\,[\hat{x}(t), \hat{p}]\right)^\dagger \tag{5}$$

The expression in eq. (5) is an example for an OTOC. It is called out-of-time-ordered because terms of the form $\hat{x}(t)\hat{p}\hat{x}(t)\hat{p}$ appear. In general, given two local operators $\hat{V}$ and $\hat{W}$ in Heisenberg picture, the combined operator

$$\left[\hat{W}(t), \hat{V}\right] \cdot \left[\hat{W}(t), \hat{V}\right]^\dagger$$

is referred to as OTOC.

From this definition it is clear that OTOCs cannot be directly measured: We need some kind of time machine to be able to evolve the system to time t and then move it backwards in time to t_0. One way to accomplish this are so-called time-reversal schemes: Given the Hamiltonian $\mathcal{H}$ of the system, the experimentalist has to implement the exact negative of the Hamiltonian to mimic the evolution backwards in time:

$$U(t_0, t_1) = e^{-i\mathcal{H}(t_1 - t_0)} \leftrightarrow e^{-i(-\mathcal{H})(t_1 - t_0)} = e^{-i\mathcal{H}(t_0 - t_1)} \equiv U(t_1, t_0). \tag{6}$$

In the case of a spin 1 spinor BEC that I study here this can be achieved by shifting all atoms from the $F = 1$ to the $F = 2$ levels, see section 2.3 for details.

2.2 Technical Framework

To be able to (mathematically) describe our system of interest, i.e. spinor dynamics in a Bose Einstein condensate (BEC) of ^{87}Rb, we first need to settle some basic terms.

A BEC is a state of matter occurring when a dilute gas of bosons is cooled down to temperatures of typically some tens of nano Kelvin. What makes the system particularly interesting for studying quantum mechanics, is the fact that almost all particles are in their motional ground state which allows the observation of quantum phenomena such as wavefunction interference or - as is the case here - spinor dynamics.

It is convenient to describe spinor dynamics in a BEC using operators in the "second quantized form" acting on a Fock basis representation: The theoretical model presented here is valid for spin 1 atoms, e.g. ^{87}Rb. For most calculations we consider our atoms to be in one of the hyperfine states $|F = 1, m_F = -1, 0, 1\rangle$. For the time reversal scheme it will be necessary to shift all atoms from the $|F = 1\rangle$ components to the corresponding $|F = 2\rangle$ components, but it will always be sufficient to consider only three m_F substates. Therefore we write our Fock states as $|N_{-1}, N_0, N_1\rangle$ where N_i represents the number of atoms in the $m_F = i$ state.

In the theoretical description we will assume that the atoms in each hyperfine component share a single spatial mode. This so-called "single mode approximation" (SMA) leaves us only with the internal degrees of freedom of our system, i.e. the spinor dynamics. How the SMA is carried out in our system is described in section 2.3.

The "second quantized form" or "occupation number representation" that we are using here is especially convenient to use for describing quantum many body systems: In the Fock basis described above we have the following basic operators:

$$\hat{a}_i^\dagger \, |N_i\rangle = \sqrt{N_i + 1} \, |N_i + 1\rangle \tag{7}$$

is the creation operator whereas a_i is the annihilation operator of the $m_F = i$ state:

$$\hat{a}_i \, |N_i\rangle = \sqrt{N_i} \, |N_i - 1\rangle \, . \tag{8}$$

They obey the bosonic commutation relations

$$[\hat{a}_i^\dagger, \hat{a}_j^\dagger] = 0 = [\hat{a}_i, \hat{a}_j] \ , \ [\hat{a}_i, \hat{a}_j^\dagger] = \delta_{ij} \tag{9}$$

From these operators we can now construct the number operators

$$\hat{N}_i \equiv \hat{a}_i^\dagger \hat{a}_i \ , \ \hat{N}_i \left|N_i\right\rangle = N_i \left|N_i\right\rangle \tag{10}$$

A natural basis to represent the state of a spin-1 particle is the "SU(3) cartesian dipole–quadrupole basis, consisting of the three components of the spin vector, S_a, and the moments of the rank-2 quadrupole or nematic tensor, Q_{ab} $(a, b \in x, y, z)$" [12]. Using the definitions for S_a and Q_{ab} given in [13]

$$\begin{aligned} S_a &= -i\hbar\epsilon_{abc}c_{bc} \\ Q_{ab} &= -c_{ab} - c_{ba} + \frac{2}{3}\delta_{ab}c_{cc} \end{aligned} \tag{11}$$

(summing over repeated indices) where $c_{ab} = b_a^\dagger b_b$ and (dropping the hats)

$$\begin{aligned} b_x^\dagger &= (-a_1^\dagger + a_{-1}^\dagger)/\sqrt{2} \\ b_y^\dagger &= i(a_1^\dagger + a_{-1}^\dagger)/\sqrt{2} \\ b_z^\dagger &= a_0^\dagger \end{aligned} \tag{12}$$

we find the following explicit form for a su(3) basis (setting $\hbar = 1$):

$$\begin{aligned} S_x &= \frac{1}{\sqrt{2}}\left\{(a_1^\dagger + a_{-1}^\dagger)a_0 + a_0^\dagger(a_1 + a_{-1})\right\} \\ S_y &= \frac{i}{\sqrt{2}}\left\{(-a_1^\dagger + a_{-1}^\dagger)a_0 - a_0^\dagger(-a_1 + a_{-1})\right\} \\ S_z &= (a_1^\dagger a_1 - a_{-1}^\dagger a_{-1}) = N_1 - N_{-1} \\ Q_{xz} &= \frac{-1}{\sqrt{2}}\left\{(-a_1^\dagger + a_{-1}^\dagger)a_0 + a_0^\dagger(-a_1 + a_{-1})\right\} \\ Q_{yz} &= \frac{-i}{\sqrt{2}}\left\{(a_1^\dagger + a_{-1}^\dagger)a_0 - a_0^\dagger(a_1 + a_{-1})\right\} \\ Q_{xy} &= i(-a_1^\dagger a_{-1} + a_{-1}^\dagger a_1) \\ Q_{zz} &= \frac{2}{3}(N_1 + N_{-1}) - \frac{4}{3}N_0 = \frac{2}{3}N - 2N_0 \\ Q_{yy} &= \frac{2}{3}N - (N_1 + a_1^\dagger a_{-1} + a_{-1}^\dagger a_1 + N_{-1}) \\ Q_{xx} &= \frac{2}{3}N - (N_1 - a_1^\dagger a_{-1} - a_{-1}^\dagger a_1 + N_{-1}) \end{aligned} \tag{13}$$

Note that Q_{ab} is traceless which is fulfilled because $Q_{xx} + Q_{yy} + Q_{zz} = 0$. So we have 8 $(= 3^2 - 1$, as required) independent basis elements spanning su(3).

2.3 Hamiltonian

For a Bose Einstein condensate in an external magnetic field, the Hamiltonian takes the form [14, 15]

$$H = \int d\vec{r} \sum_{m=-F}^{F} \psi_m^\dagger(\vec{r}) \left(\frac{-\hbar^2}{2M}\nabla^2 + U(r) - pm + qm^2 \right) \psi_m(\vec{r}) + H_{int} \tag{14}$$

where apart from the kinetic term, there is an external potential $U(r)$ and contributions from the linear ($-pm$) and quadratic (qm^2) Zeeman shift. As we can consider the dynamics in the rotating frame, see also section 3.3, we can neglect the contribution from the linear Zeeman shift in the following. The parameter $q = \mu_B^2 B_z^2/(\hbar^2 E_{HFS})$ describes the quadratic Zeeman shift due to the magnetic field B_z chosen to be along the z-axis. Here, μ_B is the Bohr magneton and E_{HFS} is the ground state hyperfine splitting.

For $F = 1$, considering only s-wave scattering, the interaction part of the Hamiltonian reads [16]

$$\begin{aligned} H_{\text{int}} = \frac{1}{2}\int d\vec{r} \; \Big[& (c_0 + c_1)(\psi_1^\dagger\psi_1)^2 + c_0(\psi_0^\dagger\psi_0)^2 + (c_0 + c_1)(\psi_{-1}^\dagger\psi_{-1})^2 \\ & + 2(c_0 + c_1)\psi_0^\dagger\psi_0(\psi_1^\dagger\psi_1 + \psi_{-1}^\dagger\psi_{-1}) + 2(c_0 - c_1)\psi_1^\dagger\psi_1\psi_{-1}^\dagger\psi_{-1} \\ & + 2c_1({\psi_0^\dagger}^2\psi_1\psi_{-1} + \psi_1^\dagger\psi_{-1}^\dagger\psi_0^2)\Big] \end{aligned} \tag{15}$$

Here, c_0 and c_1 are the spin-independent and spin-dependent coupling constants, respectively and all field operators depend on the position, so $\psi_i \equiv \psi_i(\vec{r})$.

Now, in the single mode approximation we approximate $\psi_i(\vec{r}) \approx \psi(\vec{r}) \cdot a_i$ where a_i is the bosonic Fock state annihilation operator for the $m_F = i$ state. This leads to (dropping constant terms $\propto c_0$)

$$H_{\text{int}} = \int d\vec{r} \, |\psi(r)|^4 \; 2c_1 \left[N_0(N_1 + N_{-1}) + \frac{1}{2}(N_1 - N_{-1})^2 + (a_0^\dagger a_0^\dagger a_1 a_{-1} + h.c.) \right] \tag{16}$$

where $N_i = a_i^\dagger a_i$ and $h.c.$ denotes the hermitian conjugate. That is, using the single mode approximation in the Fock space representation from above, the internal dynamics in the BEC can be described by the following Hamiltonian:

$$H = g\left\{ (a_0^\dagger a_0^\dagger a_1 a_{-1} + a_1^\dagger a_{-1}^\dagger a_0 a_0) + N_0(N_1 + N_{-1}) + \frac{1}{2}(N_1 - N_{-1})^2 \right\} + q(N_1 + N_{-1}), \tag{17}$$

where $g = 2c_1 \int d\vec{r}\ |\psi(\vec{r})|^4$ with the spin dependent coupling constant c_1 (which is negative for the $F = 1$ (ferromagnetic) and positive for the $F = 2$ state (antiferromagnetic) of ^{87}Rb).
Summarizing, the system is described by the two parameters g and q, characterizing the inter-spin and quadratic Zeeman energies, respectively.

Experimentally, the coupling g can be controlled by the density of the condensate and q can be influenced by applying an external magnetic field together with microwave dressing corresponding to an off-resonant coupling between $|F = 1, m_F = 0\rangle$ and $|2, 0\rangle$ [17].

Important to note is also that we experimentally have the possibility to apply a radio-frequency (rf) field coupling the $m_F = 0$ mode to the side modes ($m_F = \pm 1$) giving an additional term in the Hamiltonian proportional to S_x or S_y respectively. From the form of the Hamiltonian it is clear that it conserves both the total number of atoms $N = N_{-1} + N_0 + N_1$ and the "magnetization" or "imbalance" $M = N_1 - N_{-1}$. This will be of importance later, when we try to find chaotic behaviour in the classical mean field, see section 3.3.

3 Classical Mean field

In this part of my thesis I will construct the mean field equations of motion (e.o.m.) corresponding to the quantum theory described by the Hamiltonian in eq. (17). The idea is to find chaotic regions in the phase-/parameter space so that it can be checked whether e.g. OTOCs reproduce the same chaotic regions as given in the classical limit. To be able to do this, we fist have to derive the mean field equations of motion.

3.1 Derivation of the Mean Field Equations of Motion

Before we actually perform the mean field approximation, we compute the Heisenberg equations of motions for the operators a_i:

$$\begin{aligned} i\hbar\dot{a}_1 &= [a_1, H] \\ &= g\left\{\left[a_1, a_1^\dagger\right] a_{-1}^\dagger a_0 a_0 + N_0\left[a_1, a_1^\dagger\right] a_1 + \frac{1}{2}\left[a_1, N_1^2\right] - \left[a_1, a_1^\dagger\right] a_1 N_{-1}\right\} + q\left[a_1, a_1^\dagger\right] a_1 \\ &= g\left\{a_{-1}^\dagger a_0^2 + N_0 a_1 + \frac{1}{2} 2N_1 a_1 - a_1 N_{-1}\right\} + q a_1 \\ &= q a_1 + g\left\{(N_1 + N_0 - N_{-1}) a_1 + a_{-1}^\dagger a_0^2\right\} \end{aligned} \tag{18}$$

where we used that $[a_i, N_i^2] = 2N_i a_i$.
Similarly, using $\left[a_0, a_0^\dagger a_0^\dagger\right] = 2a_0^\dagger$, we get

$$i\hbar\dot{a}_0 = g\left\{a_0(N_1 + N_{-1}) + 2a_0^\dagger a_1 a_{-1}\right\} \tag{19}$$

and

$$i\hbar\dot{a}_{-1} = q a_{-1} + g\left\{(-N_1 + N_0 + N_{-1}) a_{-1} + a_1^\dagger a_0^2\right\} \tag{20}$$

Now, in the mean field approximation we treat the operators as uncorrelated in the sense that $\langle a_i a_j\rangle = \langle a_i\rangle \langle a_j\rangle$. Defining $\zeta_i \equiv \frac{1}{\sqrt{N}}\langle a_i\rangle$, such that $\zeta_i \in \mathbb{C}$, the Heisenberg equations of motion (eq. (18) to (20)) yield

$$\begin{aligned} i\hbar\dot{\zeta}_1 &= q\ \zeta_1 + gN\left\{(\rho_1 + \rho_0 - \rho_{-1})\zeta_1 + \zeta_{-1}^\star \zeta_0^2\right\} \\ i\hbar\dot{\zeta}_0 &= gN\left\{(\rho_1 + \rho_{-1})\zeta_0 + 2\zeta_0^\star \zeta_1 \zeta_{-1}\right\} \\ i\hbar\dot{\zeta}_{-1} &= q\ \zeta_{-1} + gN\left\{(-\rho_1 + \rho_0 + \rho_{-1})\zeta_{-1} + \zeta_1^\star \zeta_0^2\right\} \end{aligned} \tag{21}$$

where $\rho_i \equiv N_i/N = |\zeta_i|^2$ and a factor of $1/\sqrt{N}$ was cancelled on both sides.
Note that in the following classical calculations we will use $\tilde{g} \equiv gN$ as a parameter instead of g. This "normalization" is applied to make the mean field equations independent of the total atom number N.

3.2 Visualizations

As mentioned before (see section 2.2) the system can be described in the SU(3) space that is spanned by the eight dipole-quadrupole basis operators. Clearly, it is not possible to visualize / plot the dynamics in all of these eight dimensions simultaneously. What we can do however is to limit ourselves to SU(2) subspaces which can be visualized e.g. on Bloch spheres.

SU(2) subspaces

In order to visualise the SU(3) space on (SU(2)-) Bloch spheres, we want to find SU(2) subspaces of our original SU(3) space. To do so, we have a look at the commutators of our dipole-quadrupole basis elements and note for example that

$$\begin{aligned} [S_x, Q_{yz}] &= 2i\frac{Q_{zz} - Q_{yy}}{2} \\ \left[\frac{Q_{zz} - Q_{yy}}{2}, S_x\right] &= 2iQ_{yz} \\ \left[Q_{yz}, \frac{Q_{zz} - Q_{yy}}{2}\right] &= 2iS_x. \end{aligned} \tag{22}$$

So, e.g. $\left\{S_x, Q_{yz}, \frac{Q_{zz}-Q_{yy}}{2}\right\}$ form a SU(2) subspace of our initial phase space.
To understand the dynamics of the system (and also to check if the numerical calculations are consistent with [12]) we have a look at the mean field e.o.m. in eq. (21). Integrating them numerically in python for the initial states

$$\zeta_{init} = \exp\left(-iQ_{yz}\varphi\right)|0, 1, 0\rangle \tag{23}$$

for φ running from 0 to π in steps of $\pi/20$ and plotting the results on the $\left\{S_x, Q_{yz}, \frac{Q_{zz}-Q_{yy}}{2}\right\}$-sphere we get the trajectories shown in fig. 1.

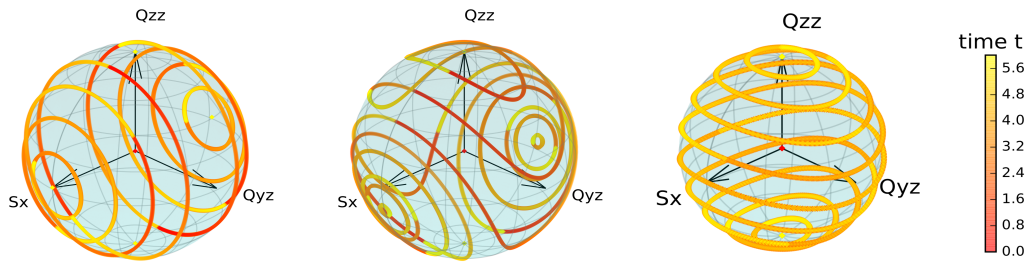

(a) $q = 0.0$ (b) $q = 0.5$ (c) $q = 5.0$

Figure 1: Mean field dynamics: Evolution until $t = 6$ for different values of the Zeeman coupling q. The inter-spin coupling constant is set to $\tilde{g} = 1$, $E_0 = 0$, $E_1 = E_{-1} = q$, leaving us with q as the only free parameter ($\hbar = 1$). The axis label denoted as Q_{zz} above is actually $-\frac{Q_{zz}-Q_{yy}}{2}$, where the minus sign has no further significance, except for being consistent with [12]. Note that the dipole-quadrupole operators have been normalised to 1, so e.g. $S_z = \left\{\zeta_0^\star(\zeta_1 + \zeta_{-1}) + \zeta_0(\zeta_1^\star + \zeta_{-1}^\star)\right\}/\sqrt{2}$ such that the e.o.m. do not depend on the total particle number N.

We note that there are two unstable fixed points at the poles ($Q_{zz} = \pm 1$) and (up to) two additional (stable) fixed points depending on the value of q. To understand fig. 1 it is useful to write the Hamiltonian as $H = \frac{g}{2}(S^2 - 2N) + pS_z + \frac{q}{2}Q_{zz}$, see e.g. [12], where in our case $p = 0$ as we consider the dynamics in the rotating frame. That means that for large q the Hamiltonian is approx. $H \propto Q_{zz}$ which results in a rotation around the Q_{zz}-axis, see fig. 1c. To understand fig. 1a we note that in the presented subspace S_y and S_z are not shown, i.e. $H \propto S^2 \propto S_x^2$ for $q = 0$ (remember $N = const$ and $S^2 = S_x^2 + S_y^2 + S_z^2$).

Re-parametrization

Alternatively, to get a simpler visualization of the dynamics, we can again have a look at eq. (21). First of all, the whole system is described by three complex fields (the components of ζ), so our phase space actually has "only" six dimensions: $\zeta_j \equiv \sqrt{\rho_j}\ e^{i\Theta_j}$. We further note, that the Hamiltonian in eq. (17) conserves the particle number N. Additionally, we can transform into a rotating frame, e.g. by choosing the phase of ζ_0 to be zero $\Theta_0 \equiv 0$, i.e. making ζ_0 real. This

amounts to fixing a global phase which we are always allowed to do as a global phase cannot be measured and does not influence the dynamics. Introducing a normalized "magnetization" $m = (N_1 - N_{-1})/N$ along with the Larmor precession phase $\Theta_m = \Theta_1 - \Theta_{-1}$ and the spinor phase (defined such that $\Theta_0 \equiv 0$) $\Theta_s = \Theta_1 + \Theta_{-1} - 2\Theta_0$ we can write ζ as (see also [13])

$$\begin{aligned} \zeta_1 &= \sqrt{\frac{1-\rho_0+m}{2}}\; e^{i\frac{\Theta_s+\Theta_m}{2}} \\ \zeta_0 &= \sqrt{\rho_0} \\ \zeta_{-1} &= \sqrt{\frac{1-\rho_0-m}{2}}\; e^{i\frac{\Theta_s-\Theta_m}{2}} \end{aligned} \tag{24}$$

With this parametrisation, the mean field time evolution from fig. 1 looks like:

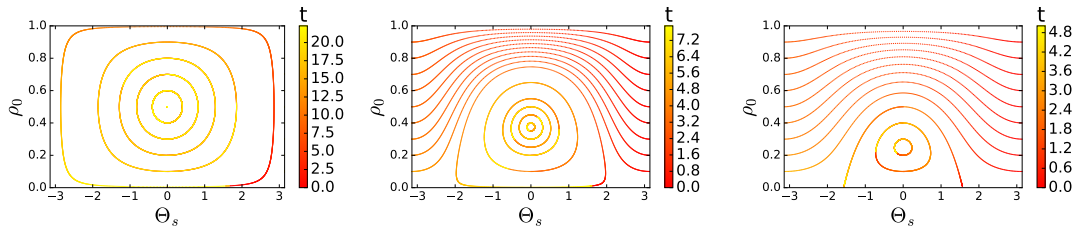

(a) $q = 0.0$ (b) $q = 0.5$ (c) $q = 1.0$

Figure 2: Mean field dynamics: Time evolution for different values of the Zeeman coupling q shown in $\{\rho_0, \Theta_s\}$ phase space. The whole phase space includes also m and Θ_m but they are not shown as m is conserved and Θ_s is cyclic, see section 3.3. The inter-spin coupling constant is set to $\tilde{g} = 1$, $E_0 = 0$, $E_1 = E_{-1} = q$, leaving us with q as the only free parameter ($\hbar = 1$).

3.3 Modifying the Hamiltonian to find chaos

Until now we examined the dynamics of our system in different representations. But looking at fig. 1 and fig. 2 we see very regular, i.e. non-chaotic behaviour. To understand why there are apparently no chaotic regions, we again have a look at the Hamiltonian in eq. (17). By substituting the mean field approximated $\zeta_i \equiv \frac{1}{\sqrt{N}} \langle a_i \rangle$ we get the classical energy functional

$$\mathcal{E} \equiv E/N = gN \left\{ \zeta_0^{*2}\zeta_1\zeta_{-1} + \zeta_1^*\zeta_{-1}^*\zeta_0^2 + |\zeta_0|^2 \left(|\zeta_1|^2 + |\zeta_{-1}|^2 \right) + \frac{1}{2}m^2 \right\} + q \left(|\zeta_1|^2 + |\zeta_{-1}|^2 \right) \tag{25}$$

where we used that $m = (N_1 - N_{-1})/N = \rho_1 - \rho_{-1}$.

Furthermore, using normalisation, i.e. $1 = \rho_1 + \rho_0 + \rho_{-1} \Leftrightarrow |\zeta_1|^2 + |\zeta_{-1}|^2 \equiv \rho_1 + \rho_{-1} = 1 - \rho_0$ and the parametrisation of ζ from eq. (24), we arrive at

$$\begin{aligned}\mathcal{E} &= \frac{gN}{2}m^2 + gN\rho_0\left\{(1-\rho_0) + \frac{1}{2}\sqrt{(1-\rho_0)^2 - m^2}\; e^{i\Theta_s} + \frac{1}{2}\sqrt{(1-\rho_0)^2 - m^2}\; e^{-i\Theta_s}\right\} \\ &\quad + q\,(1-\rho_0) \\ &= \frac{gN}{2}m^2 + gN\rho_0\left\{(1-\rho_0) + \sqrt{(1-\rho_0)^2 - m^2}\;\cos\Theta_s\right\} + q\,(1-\rho_0)\end{aligned} \tag{26}$$

The interesting thing about the energy functional (26) is that Θ_m does not appear, i.e. it is a cyclic variable. Furthermore, we know that $\dot{m} = 0$ because S_z commutes with the Hamiltonian and thus also in the mean field e.o.m. m has to be conserved.

Hence we have seen that the phase space in terms of $\{\rho_0, \Theta_s, m, \Theta_m\}$ is only two dimensional in the sense that non-trivial dynamics only include $\{\rho_0, \Theta_s\}$. According to the Poincaré-Bendixson theorem [18] chaos can only arise in continuous dynamical systems if the phase space has three or more dimensions. This explains why we cannot find chaos in the system described by the Hamiltonian in eq. (17). In order to observe chaotic behaviour, we have to increase the dimensionality of our "effective" phase space. One way to achieve this is to modify the Hamiltonian such that m is not conserved any more.

We want to do this by adding a time-independent (non driven) term to the Hamiltonian, such that we do not break energy conservation symmetry. Experimentally, we have the options to apply radio-frequency (rf) pulses resonant with the transition $|1,0\rangle \leftrightarrow |1,\pm1\rangle$ that can be modelled by constant S_x or S_y terms in the Hamiltonian within a rotating wave approximation (we transform into a frame rotating with the frequency corresponding to the linear Zeeman shift). Here, I choose to add a S_x term to the Hamiltonian (S_y works as well):

$$H_c := H + r \cdot S_x \;,\; r \in \mathbb{R} \tag{27}$$

Remember that

$$S_x = \frac{1}{\sqrt{2}}\left\{(a_1^\dagger + a_{-1}^\dagger)a_0 + a_0^\dagger(a_1 + a_{-1})\right\} \;. \tag{28}$$

In order to calculate the new mean field e.o.m. for ζ, we first have a look at the commutators with S_x:

$$\begin{aligned}
[a_1, S_x] &= \frac{1}{\sqrt{2}}\left[a_1, a_1^\dagger\right] a_0 = \frac{1}{\sqrt{2}} a_0 \\
[a_0, S_x] &= \frac{1}{\sqrt{2}}\left[a_0, a_0^\dagger\right] (a_1 + a_{-1}) = \frac{1}{\sqrt{2}}(a_1 + a_{-1}) \\
[a_{-1}, S_x] &= \frac{1}{\sqrt{2}}\left[a_{-1}, a_{-1}^\dagger\right] a_0 = \frac{1}{\sqrt{2}} a_0
\end{aligned} \tag{29}$$

Knowing the new part of the Heisenberg e.o.m. for the annihilation operators a_i we can write down the modified mean field e.o.m. (compare to eq. (21)):

$$\begin{aligned}
i\hbar\dot{\zeta}_1 &= q\ \zeta_1 + gN\left\{(\rho_1 + \rho_0 - \rho_{-1})\zeta_1 + \zeta_{-1}^\star \zeta_0^2\right\} + \frac{r}{\sqrt{2}}\ \zeta_0 \\
i\hbar\dot{\zeta}_0 &= gN\left\{(\rho_1 + \rho_{-1})\zeta_0 + 2\zeta_0^\star \zeta_1 \zeta_{-1}\right\} + \frac{r}{\sqrt{2}}\ (\zeta_1 + \zeta_{-1}) \\
i\hbar\dot{\zeta}_{-1} &= q\ \zeta_{-1} + gN\left\{(-\rho_1 + \rho_0 + \rho_{-1})\zeta_{-1} + \zeta_1^\star \zeta_0^2\right\} + \frac{r}{\sqrt{2}}\ \zeta_0
\end{aligned} \tag{30}$$

Modified Energy Functional

If we want to examine the dynamics in the $\{\rho_0, \Theta_s, m, \Theta_m\}$ space, it is also useful to calculate the modified energy functional. The energy functional corresponding to S_x is

$$\begin{aligned}
\mathcal{E}_{S_x} &= \frac{1}{\sqrt{2}}\left\{\left(\sqrt{\frac{1-\rho_0+m}{2}} e^{-i\frac{\Theta_s+\Theta_m}{2}} + \sqrt{\frac{1-\rho_0-m}{2}} e^{-i\frac{\Theta_s-\Theta_m}{2}}\right)\sqrt{\rho_0}\right. \\
&\quad \left. +\ \sqrt{\rho_0}\left(\sqrt{\frac{1-\rho_0+m}{2}} e^{i\frac{\Theta_s+\Theta_m}{2}} + \sqrt{\frac{1-\rho_0-m}{2}} e^{i\frac{\Theta_s-\Theta_m}{2}}\right)\right\} \\
&= \frac{\sqrt{\rho_0}}{2}\left\{\sqrt{1-\rho_0+m}\left(e^{i\frac{\Theta_s+\Theta_m}{2}} + e^{-i\frac{\Theta_s+\Theta_m}{2}}\right) + \sqrt{1-\rho_0-m}\left(e^{i\frac{\Theta_s-\Theta_m}{2}} + e^{-i\frac{\Theta_s-\Theta_m}{2}}\right)\right\} \\
&= \sqrt{\rho_0}\left\{\sqrt{1-\rho_0+m}\ \cos\left(\frac{\Theta_s+\Theta_m}{2}\right) + \sqrt{1-\rho_0-m}\ \cos\left(\frac{\Theta_s-\Theta_m}{2}\right)\right\}
\end{aligned} \tag{31}$$

Thus, the modified energy functional is

$$\begin{aligned}
\mathcal{E}_{\mathrm{c}} &= \mathcal{E} + r \cdot \mathcal{E}_{S_x} \\
&= \frac{gN}{2} m^2 + gN\rho_0\left\{(1-\rho_0) + \sqrt{(1-\rho_0)^2 - m^2}\ \cos\Theta_s\right\} + q\,(1-\rho_0) \\
&\quad + r\sqrt{\rho_0}\left\{\sqrt{1-\rho_0+m}\ \cos\left(\frac{\Theta_s+\Theta_m}{2}\right) + \sqrt{1-\rho_0-m}\ \cos\left(\frac{\Theta_s-\Theta_m}{2}\right)\right\}
\end{aligned} \tag{32}$$

Simulation of Modified Mean Field Equations

Since the mean field equations of motion for ρ_0, Θ_s, Θ_m and m will be very bulky, we keep working in the ζ parametrization for convenience, see eq. (30). But still we want to visualise the classical trajectories in the $\{\rho_0, \Theta_s, m, \Theta_m\}$ phase space, therefore we need a mapping between these two representations. One direction is given by eq. (24) and the other can be found by inverting this equation, but only after fixing the global phase: ζ has the general form $\zeta_i \equiv \sqrt{\rho_i}\, e^{i\Theta_i}$. We now transform to $\tilde{\zeta}_i = \zeta_i \cdot e^{-i\Theta_0}$ such that Arg $\tilde{\zeta}_0 = 0$, i.e. $\tilde{\zeta}_0 \in \mathbb{R}$. Now we can get back ρ_0, Θ_s, m and Θ_m as follows:

$$\begin{aligned} \rho_0 &= \tilde{\zeta}_0^{\,2} \\ m &= |\tilde{\zeta}_1|^2 - |\tilde{\zeta}_{-1}|^2 \\ \Theta_s &= \text{Arg } \tilde{\zeta}_1 + \text{Arg } \tilde{\zeta}_{-1} \\ \Theta_m &= \text{Arg } \tilde{\zeta}_1 - \text{Arg } \tilde{\zeta}_{-1} \end{aligned} \tag{33}$$

To see whether the numerical integration of the modified classical e.o.m. work, we check that the norm ($|\zeta| = 1$) and the total energy (eq. 32) are conserved, see fig. 3.

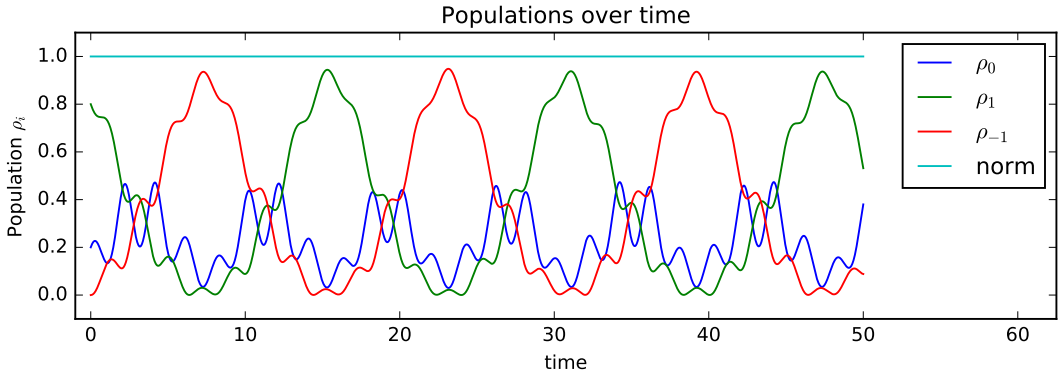

Figure 3: Populations of the different m_F states over time for $\tilde{g} = q = 1$, $r = 0.7$. The norm is calculated as the sum of all populations. The total energy is conserved up to a relative error $\Delta E < 10^{-4}$.

3.4 Poincaré Maps

In order to visualize the dynamics produced by the modified (still classical) Hamiltonian (see previous section 3.3) we have to employ some new techniques: Because of the broken m symmetry, the system does not stay on the surface of the SU(2) Bloch spheres any more, that have been used before to visualize the dynamics. Although this is still a valid visualization, it can not be easily interpreted any more. But even if we use the parametrization of ζ in terms of ρ_0, m, Θ_s and Θ_m, we run into problems: Due to the fact that m is not conserved any more, the dynamics now take place in an effectively four dimensional phase space.

To "reduce" the dimensionality of the visualization we will proceed as follows: First, we use the fact that our perturbation term is constant in time (in contrast to e.g. the periodically driven system in ref. [2]) so that the total energy is conserved. I.e., after fixing a total energy, the system will stay on a three dimensional "surface", subset to the original four dimensional phase space. Although it is in principle possible to plot three dimensional trajectories, it is not easy to distinguish between chaotic and regular behaviour in such a representation. To reduce the dimensionality once again, we use a technique called Poincaré maps or Poincaré sections:

In general, a Poincaré section of a dynamical system in N dimensional phase space is defined as a $(N-1)$ dimensional surface of section. I.e. instead of looking at the N dimensional trajectories directly, we only record the points where the trajectories pierce through a $(N-1)$ dimensional (hyper-) surface. For simpler systems these maps can be analytically calculated but in most cases (as in ours) they have to be computed numerically, i.e. they are really rather sections than maps.

In our case we have a 4-dimensional phase space and we define our 3-dimensional section by the equation $\Theta_m = 0$. Instead of representing the solutions to the e.o.m. as trajectories in 4-dim. phase space (which is pretty hard to visualise), we look at consecutive intersections with our 3-dim. subset defined by $\Theta_m = 0$.

There is a very nice scheme how to find these points of intersections exactly [19]: After each integration step the section defining equation (here: $\Theta_m = 0$) is evaluated. For this scheme, we require the plane of section to be perpendicular

to one of the coordinate axes x_N, (which is given in our case, $x_N = \Theta_m$). This can always be achieved by rotating the coordinate system. When a change of sign is detected, we change our equations of motion such that x_N becomes the independent variable by dividing all equations $f_i(y, x)$ by f_N. Now the formerly independent variable (time) becomes a dependent one. As x_N is now independent, we can exactly integrate back to the surface of section be choosing the step size as Θ_m. Once we found our point of intersection, we change back to the original system of equations and proceed with the integration.

When implementing this procedure, I ran into a lot of numerical instabilities. That is why I used a much simpler and slightly more imprecise scheme: First, I integrate the system and record the four dimensional coordinates at every time step. Then, I check for (smooth) zero crossings of Θ_m and simply linearly interpolate between the two adjacent points. By making the integration steps sufficiently small (what I have to do anyway to ensure energy conservation up to a relative error of the order $1e-4$), the points of intersection can be determined arbitrarily precisely.

We are now left with three dimensions. But as mentioned above, the total energy is conserved, so that we can project the 3d plot onto two dimensions. We choose ρ_0 and Θ_s here to directly see how the Poincaré sections change from the unperturbed phase space picture when we slowly turn up the disturbance parameter r.

It is certainly true that we loose information by only looking at the Poincaré sections compared to the four dimensional trajectories. But as our aim is to determine for what parameters and initial states the system exhibits chaotic behaviour, it is enough to look at Poincaré sections: When the intersection points are strictly confined in a (one dimensional) subspace of the section, dynamics are regular. When the points of intersection are instead spread over a larger area (only limited by conservation of energy and norm) then the system is topologically mixing and very likely to be chaotic.

Implementation

A few words concerning the actual implementation: For a given set of initial values $\{\rho_0, m, \Theta_s, \Theta_m\}$ we convert them to ζ according to eq. (24). Then the equations of motion for ζ are numerically integrated to calculate its time evolution. After that, at each recorded point in time, ζ is converted back to $\{\rho_0, m, \Theta_s, \Theta_m\}$ and in this representation we check for (smooth) zero crossings in Θ_m. We can now record the interpolation between the points where the zero crossing happened as described above. In the end we want to plot a raster of different initial values matching a given total energy E. In order to achieve this, we sample ρ_0 and Θ_s and try to find a value of Θ_m such that the initial states match the energy E for $m = 0.1$. If this is not successful, we vary m from $-\rho_0$ to ρ_0 and try to find Θ_m corresponding to E. In order to find a value of $\Theta_m = \Theta_m(\rho_0, m, \Theta_s, E, g, q, r)$ we have to invert the energy functional given in eq. (32). To do so, we first write it as

$$E = f(\rho_0, m, \Theta_s) + r\sqrt{\rho_0}\left\{A\cos\left(\frac{\Theta_s - \Theta_m}{2}\right) + B\cos\left(\frac{\Theta_s + \Theta_m}{2}\right)\right\} \tag{34}$$

where $A = \sqrt{1 - \rho_0 - m}$, $B = \sqrt{1 - \rho_0 + m}$ such that A, B and f do not depend on Θ_m. Solving this equation for Θ_m gives

$$\Theta_m = \pm 2 \arccos\left\{\frac{\pm\sqrt{(A+B)^2(A^2+B^2-C^2+2AB\cos\Theta_s)\sin^2\frac{\Theta_s}{2}} + (A-B)C\sin\frac{\Theta_s}{2}}{A^2+B^2+2AB\cos\Theta_s}\right\} \tag{35}$$

where $C = \frac{E - f(\rho_0, m, \Theta_s)}{r\sqrt{\rho_0}}$.

It is obvious that this expression is not well defined for $r = 0$ or $\rho_0 = 0$. But this is not surprising because in these cases E does not depend on Θ_m, i.e. for some energy E, all values of Θ_m are valid solutions to the problem. If this happens, the subroutine implementing eq. (35) returns a set of several values between $-\pi$ and π.

Results

Our aim is to find chaotic regions depending on a set of parameters, most importantly on the disturbance r. To produce the plots in fig. 4, we set $\tilde{g} = q = 1$, vary r and plot the Poincaré sections with the surface defined by $\Theta_m = 0$ for different initial states.

We see that in the case of $r = 0$ the points belonging to each Poincaré section form closed contours, indicating regular behaviour, see fig. 4a. Note that in this figure we plotted Poincaré sections for initial states corresponding to different energies to be able to show dynamics in a larger region of the phase space. As we expect, fig. 4a resembles the phase space picture for the unperturbed system shown above in fig. 2c.

If we now increase the disturbance to $r = 0.15$, see fig. 4b and 4c, we see that there are regular regions as well as regions where no closed contours can be seen. In these latter regions the classical mean field e.o.m. produce chaotic behaviour. In the left picture it is shown that the Poincaré sections corresponding to initial states with small ρ_0 become chaotic sooner than those starting at larger values of ρ_0. This is expected because $\rho_0 = 0$ is an unstable fixed point of the unperturbed dynamics. Further increasing r, we see that all energetically accessible regions in phase space show chaotic behaviour. If we increase r even more, new regular patterns emerge. This is because for large r, the Hamiltonian is approximately proportional to S_x which results again in a regular phase space.

This is what we hoped to find: Starting with the unperturbed Hamiltonian, we get regular behaviour. Turning up r results first in a mixed phase space where only parts of it show chaotic behaviour. Increasing the perturbation even more results in a completely chaotic phase space where no more regular regions are visible. Only for higher values of r regular patterns re-emerge.

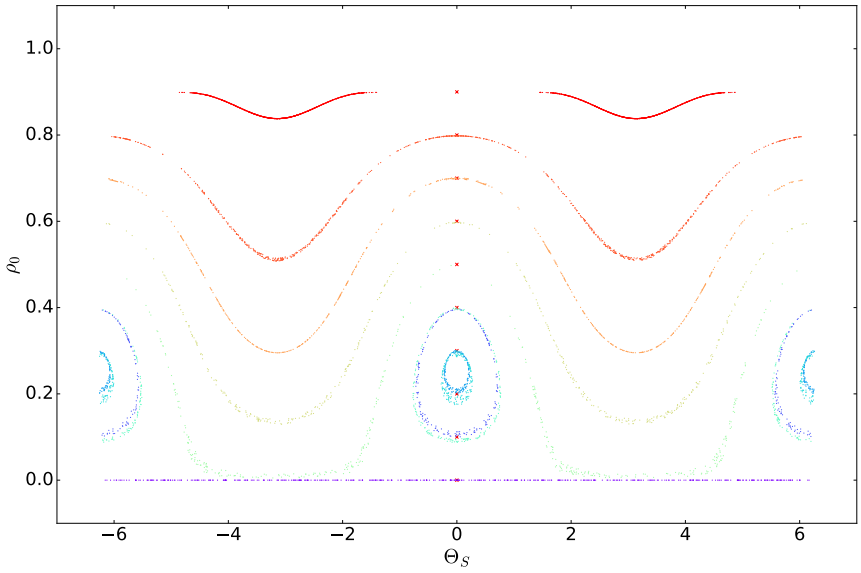

(a) $r = 0.00$

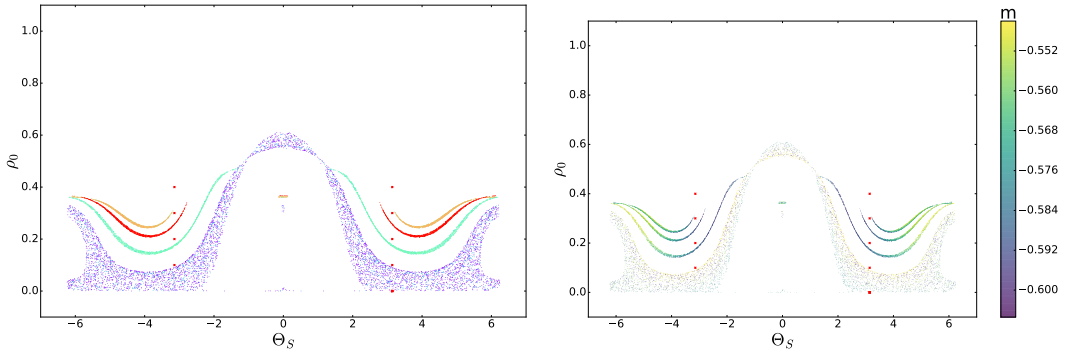

(b) $r = 0.15$ (c) $r = 0.15$

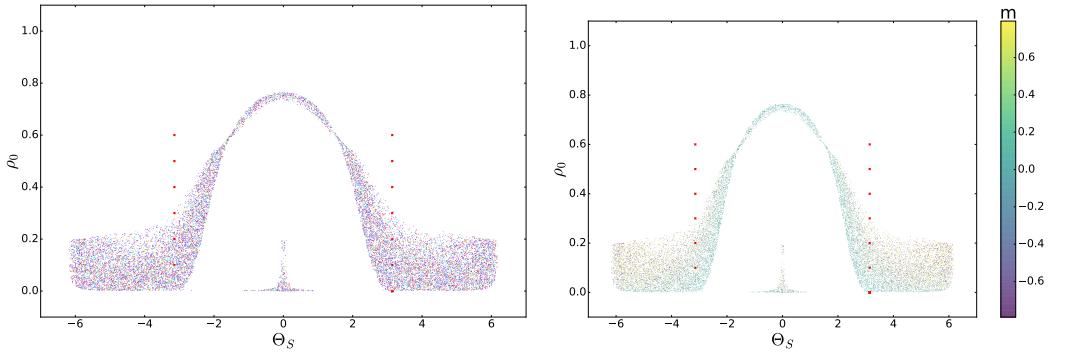

(d) $r = 0.5$ (e) $r = 0.5$

Figure 4: Poincaré maps of mean field dynamics defined by $\Theta_m = 0$. (a) initial conditions corresponding to different energies. (b) and (d) initial conditions corresponding to the same energy, each initial condition in a different colour, (c) and (e) same as (b) and (d) but the values of m at each point of intersection are colour encoded. Initial values of ρ_0 and Θ_s are marked by red crosses. All of these maps have been calculated for $\tilde{g} = q = 1$.

3.5 Lyapunov exponent

As already mentioned in section 2.1, Lyapunov exponents describe how fast two infinitesimally close trajectories diverge. A positive Lyapunov exponent implies that phase space trajectories diverge exponentially fast, i.e. in that case the system is very likely to exhibit chaotic behaviour. If $\vec{z}_1(t)$ is a trajectory and $\vec{z}_2(t) \equiv \vec{z}_1(t) + \vec{\xi}(t)$ is another, infinitesimally close trajectory, then the largest Lyapunov exponent λ can be obtained (see e.g. [20]) as

$$\lambda = \lim_{t\to\infty} \frac{1}{t} \log \frac{\left|\vec{\xi}(t)\right|}{\left|\vec{\xi}_0\right|} \ . \tag{36}$$

To numerically evaluate this limit we use a method documented in [20]: Given a starting point in phase space $\vec{z}_1(t_0)$ we choose a random point $\vec{z}_2(t_0)$ with initial separation d_0. We then calculate the time evolution for both trajectories simultaneously by numerical integration. After each time step $\log(d_1(t)/d_0)$ is evaluated and recorded, where $d_1(t) = |\vec{z}_1(t) - \vec{z}_2(t)|$. Then, a new point z_2 is chosen such that it lies in the direction of the former $\vec{z}_2(t)$ but at a distance d_0 from $\vec{z}_1(t)$. Then the integration is resumed and carried out, here until $t = 500$. In the end, the average is taken over the recorded values omitting all values up to $t = 100$. We omit the first values to ensure that we have reached the basin of attraction which is important to get a sensible estimate of the Lyapunov exponent.

Implementation

We want to calculate the Lyapunov exponents for a set of initial values such that we can compare the results to the Poincaré sections from section 3.4. That is why we choose $\Theta_m = 0$, raster over all values of ρ_0 and Θ_s and calculate the Lyapunov exponent for all $\{\rho_0, \Theta_s\}$ where we find a value of m corresponding to a given total energy E. To find $m = m(\rho_0, \Theta_s, \Theta_m, E, r, ...)$ we numerically invert eq. (32) and take only one possible value of m resulting in an energy E. We have to invert the energy functional numerically because there (probably) is no analytical way to determine m.

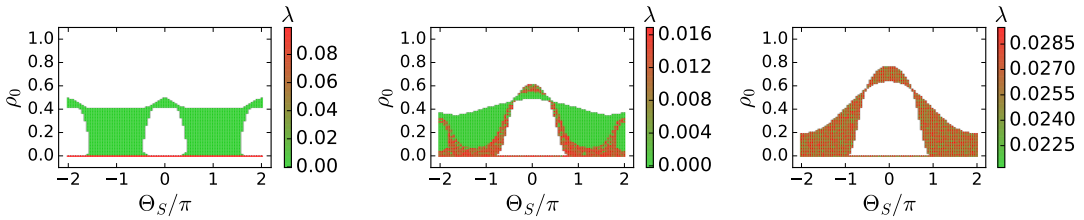

(a) $r = 0.00$

(b) $r = 0.15$

(c) $r = 0.50$

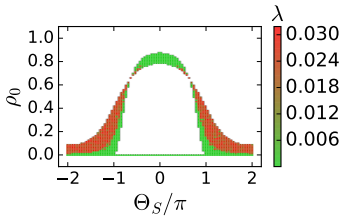

(d) $r = 1.00$

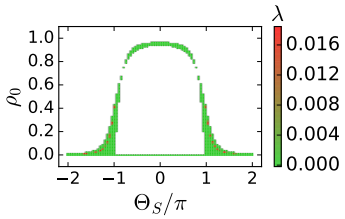

(e) $r = 2.50$

Figure 5: Lyapunov exponents λ for a raster of 80×80 values of ρ_0 and Θ_s, $\Theta_m = 0$. The value of m has been calculated to match a given energy $E = 1.005$. This energy mainly influences the allowed compatible regions in phase space. Again, $\tilde{g} = q = 1$.

For $r = 0$, see fig. 5a, all points have a Lyapunov exponent close to zero (coloured in green) corresponding to regular behaviour except the points where $\rho_0 = 0$. Classically, these points correspond to an unstable fixed point [3] which would explain why in the short time evolution these points show rapidly diverging trajectories when slightly perturbed. As we increase r we see in figures 5b and 5c that the chaotic regions, i.e. regions in phase space where the Lyapunov exponents $\lambda > 0$, grow (coloured in red). At first, we have a mixed phase space as in fig. 5b until eventually all allowed initial states lead to chaotic dynamics, see fig. 5c. Only for much larger values of r regular regions dominate again, as can be seen in fig. 5d and 5e.

Discussion of Classical Results

Setting $\tilde{g} = q = 1$, we saw that for $r \lesssim 0.15$ regular regions dominate, for $r \approx 0.15 \ldots 0.30$ we have a mixed phase space, for $r \approx 0.30 \ldots 0.85$ chaos dominates and for $r \gtrsim 0.90$ the system becomes regular again. This is the result that we obtained from the classical theory, clearly visible in both Poincaré maps and

Lyapunov exponents. The next step will be to consider the full quantum theory and see, whether we can find analogues of quantum mechanical measures that reproduce the same chaotic regions.

4 Quantum Calculations

4.1 Concept and Limitations

The Hamiltonian system we are interested in is far too complicated to be solved analytically. But as we still want to do the quantum calculations, we have to use numerical methods to solve the equations. To do so, we first compute a complete set of basis states for our Fock space: $B = \{|0, N, 0\rangle, |0, N-1, 1\rangle, \ldots, |N, 0, 0\rangle\}$ where N is the total number of atoms. That means that we have

$$|B| = \frac{(N+1)(N+2)}{2} = o(N^2)$$

basis states.

In a next step, we have to construct our operators with respect to this basis. As the total number of atoms is always conserved, we have to break the Hamiltonian down into pairs of creation / annihilation operators that conserve N (all operators which do not conserve N would have a representation matrix containing only zeros). As a set of basic operators we choose

$$\left\{a_0^\dagger a_1, a_0^\dagger a_{-1}, a_1^\dagger a_{-1}, N_i \equiv a_i^\dagger a_i, i \in \{-1, 0, 1\}\right\} . \tag{37}$$

What we mean by constructing the operators with respect to the basis B is the following: Let $|b_n\rangle, |b_m\rangle \in B$ be two basis states. Then the (m, n)-element of the matrix O representing the operator $\mathcal{O}$ is given by

$$O_{n,m} = \langle b_n | \mathcal{O} | b_m \rangle . \tag{38}$$

Once we have the representation of our basic operators, we can construct the Hamiltonian and other combinations of operators (observables) from these. If we now want to compute the time evolution of a given state $|\psi\rangle$ we have two possibilities: We can solve the system by numerically diagonalising the Hamiltonian or we can solve the differential equations for the coefficients that represent $|\psi\rangle$ with

respect to the basis B. In the first case, we numerically compute the eigenvectors $\vec{v}_i$ and the corresponding eigenvalues λ_i of the Hamiltonian matrix H defined by $H \cdot \vec{v}_i = \lambda_i \vec{v}_i,\ i = 1, \ldots, n$ where H is a $n \times n$ matrix. Bundling all eigenvectors in a matrix $V = (\vec{v}_1, \ldots, \vec{v}_n)$ containing them as column vectors, we can compute the state $|\psi(t)\rangle$ at different times t as

$$|\psi(t)\rangle = V\ diag\left(e^{-it\lambda_1}, \ldots, e^{-it\lambda_n}\right)\ V^\dagger\ |\psi(t=0)\rangle\ . \tag{39}$$

For the other possibility we write $|\psi(t)\rangle = \sum_k c_k(t)\,|b_k\rangle$ for $|b_k\rangle \in B$. To get the time evolution of $|\psi\rangle$ we have to calculate the time dependence of the coefficients c_k. To see how we can compute them, we start with the Schrödinger equation

$$i\partial_t\,|\psi\rangle = \mathcal{H}\,|\psi\rangle \tag{40}$$

where ∂_t denotes the time derivative. Multiplying both sides with $\langle b_l|$ we get

$$\dot{c_l} = \partial_t \sum_k c_k(t)\,\langle b_l|b_k\rangle = -i \sum_k c_k(t)\,\langle b_l|\mathcal{H}|b_k\rangle \tag{41}$$

where we used that basis states are orthonormal, i.e. $\langle b_l|b_k\rangle = \delta_{kl}$. We can bring these equations in a simpler form by combining the c_k's into a coefficient vector $\vec{c}$:

$$\dot{\vec{c}} = -iH\vec{c} \tag{42}$$

where H denotes the matrix representation of $\mathcal{H}$ in the above sense. Equation (42) is a system of coupled ordinary differential equations and can be integrated numerically for a given initial state.

I implemented both methods and compared their performance, i.e. how long they take to compute the time evolution of a state given the total number of atoms and the number of time steps. It turned out that both methods are more or less equally efficient. This is not what we expected but it can probably be explained by the sparseness of H: If H was a dense $n \times n$ matrix, diagonalization should scale as n^3 whereas the matrix vector multiplication used in the numerical integration should scale only as n^2 making the latter method potentially much more efficient.

Once we have the time evolution of $|\psi(t)\rangle$ we can compute observables simply by evaluating $\langle\psi(t)|O|\psi(t)\rangle$.

4.2 Coherent States

So far, I have not talked about the initial state whose time evolution I want to compute. In theory, we could pick any possible state but it makes sense to pick a state that has a well defined classical limit (as in the end, we want to compare the quantum calculations with the mean field results). A sensible choice for such states are so-called coherent states: These are states that can be expressed as product states in the following way:

$$\begin{pmatrix} \zeta_1 \\ \zeta_0 \\ \zeta_{-1} \end{pmatrix}^{\otimes N} = (\zeta_1 |1\rangle + \zeta_0 |0\rangle + \zeta_{-1} |-1\rangle)_1 \otimes (\dots)_2 \otimes \cdots \otimes (\dots)_N \tag{43}$$

where the coefficients are the same in each bracket.

Initially, I computed such states by rotating the polar state $|0, N, 0\rangle$ e.g. by an angle ϕ around S_x but this turns out to be numerically inefficient as it contains a matrix exponential:

$$|\psi_0\rangle = e^{iS_x\phi} |0, N, 0\rangle \tag{44}$$

If one observes that $(S_x)^{n+2} = (S_x)^n$ for $n \in \mathbb{N}$, one can show that

$$e^{iS_x\phi} = 1 + iS_x \sin\phi + S_x^2 (\cos\phi - 1) \tag{45}$$

which amounts to the vector Rodrigues' rotation formula [21] and hence

$$e^{iS_x\phi} |0\rangle = \cos\phi |0\rangle + \frac{i}{\sqrt{2}} \sin\phi (|1\rangle + |-1\rangle) . \tag{46}$$

This is a useful result because we can write $|0, N, 0\rangle = |0\rangle_1 \otimes \cdots \otimes |0\rangle_N$ and hence

$$\begin{aligned} e^{iS_x\phi} |0, N, 0\rangle &= e^{iS_x\phi} |0\rangle_1 \otimes \cdots \otimes |0\rangle_N \\ &= \bigotimes_{i=1}^{N} \left(\cos\phi |0\rangle_i + \frac{i}{\sqrt{2}} \sin\phi |1\rangle_i + \frac{i}{\sqrt{2}} \sin\phi |-1\rangle_i \right) \\ &= \sum_{N_{-1}, N_0, N_1} (\cos\phi)^{N_0} (\frac{i}{\sqrt{2}} \sin\phi)^{N_1} (\frac{i}{\sqrt{2}} \sin\phi)^{N_{-1}} \sum_{\text{perm}} |\dots\rangle_1 \otimes \cdots \otimes |\dots\rangle_N \\ &= \sum_{N_0 + N_1 \leq N} (\cos\phi)^{N_0} (\frac{i}{\sqrt{2}} \sin\phi)^{N - N_0} \sqrt{k} \ |N - N_0 - N_1, N_0, N_1\rangle \end{aligned} \tag{47}$$

The sum over N_{-1}, N_0, N_1 in the third line runs such that $N_{-1} + N_0 + N_1 = N$ so that N_{-1} can be expressed by N_0 and N_1 in the next line. At the end of the

third line, the sum runs over all permutations of the tensor product of the single states such that each state $|i\rangle$ appears N_i times in total for $i \in \{-1, 0, 1\}$. The normalisation of the Fock states k is given as follows: There are

$$k = \binom{N}{N_0}\binom{N-N_0}{N_1} = \frac{N!}{N_{-1}!N_0!N_1!} = \frac{N!}{(N-N_0-N_1)!N_0!N_1!} \tag{48}$$

possibilities for permutations of $|\ldots\rangle_1 \otimes \cdots \otimes |\ldots\rangle_N$ such that $|i\rangle$ appears N_i times. Hence

$$\frac{1}{\sqrt{k}} \sum_{\text{perm}} |\ldots\rangle_1 \otimes \cdots \otimes |\ldots\rangle_N = |N_{-1}, N_0, N_1\rangle \,. \tag{49}$$

We can generalize this concept in the following way: A more general method to numerically prepare any coherent state corresponding to a set of $\{\rho_0, \Theta_s, m, \Theta_m\}$, is to first convert these parameters to $\{\zeta_{-1}, \zeta_0, \zeta_1\}$ using the mapping from eq. (24) from section 3.2 and then compute the coherent state via

$$\begin{aligned} \begin{pmatrix} \zeta_1 \\ \zeta_0 \\ \zeta_{-1} \end{pmatrix}^{\otimes N} &= (\zeta_1 |1\rangle + \zeta_0 |0\rangle + \zeta_{-1} |-1\rangle)_1 \otimes (\ldots)_2 \otimes \cdots \otimes (\ldots)_N \\ &= \sum_{N_{-1},N_0,N_1} (\zeta_{-1})^{N_{-1}} (\zeta_0)^{N_0} (\zeta_1)^{N_1} \sqrt{k} \;\; |N_{-1}, N_0, N_1\rangle \end{aligned} \tag{50}$$

where $\sum_{N_{-1},N_0,N_1}$ is such that $N_{-1} + N_0 + N_1 = N$ and with the multinomial coefficient k defined in eq. (48).

Experimentally, coherent states can still be prepared by e.g. rotating the polar state but for the simulations, the numerical computation of coherent states as presented above is far more efficient.

4.3 Visualisation

To check whether the quantum calculations work and actually produce dynamics corresponding to the classical mean field evolution of the system, we want to visualize the time evolution of some initial state. In the previous section I described how to construct a coherent state corresponding to a point in classical phase space defined by $\{\rho_0, \Theta_s, m, \Theta_m\}$. I also explained how to calculate the time evolution of any given state. What is still needed is a way to visualise a "state" or more precisely a probability distribution in such a way that we can easily compare it to the phase space representation that we used for the classical states. One way

to go - conceptually straight forward but computationally rather expensive - is to project the state of interest at each time step onto a grid of coherent states. Because the classical limit of the coherent states is well defined, the overlap with these states can be interpreted as the probability to measure $\{\rho_0, \Theta_s, m, \Theta_m\}$. Note that such a measurement is of course not possible in quantum mechanics.

As already noted, this procedure is computationally rather expensive: Even if we project only on coherent states corresponding to $\Theta_m = 0$ to be able to compare with the Poincaré sections (see sec. 3.4), our grid still consists of M^3 points. Here, M is the resolution in ρ_0, Θ_s and m, i.e. the number of points that is sampled for each of these variables. If we then want to calculate the time evolution for M_T time steps, we have to construct M^3 coherent states and calculate $M^3 \cdot M_T$ overlaps. For realistic parameters of $M = 40$ and $M_T = 300$ this corresponds to roughly 2×10^7 projections. Note, that there are actually fewer than M^3 allowed states because of the normalization $|\zeta| = 1$: Only states with $|m| \leq 1 - \rho_0$ are physical states.

I did the calculations for a total atom number of $N = 10$, 30 and 60 particles to see whether the distributions get more and more peaked with increasing particle number as we would expect: For $N \to \infty$ the system should be classical in the sense that a state is specified by a point (corresponding to a Dirac distribution) in phase space.

The plots are shown in section 5.1.

4.4 Level Statistics

A well established tool to check for chaos - or to be more precise, for randomness - in quantum mechanical systems is the analysis of the level statistic of the energy eigenvalue spacings of the system [22]. A motivation, why level statistics say something about the amount of order or randomness in a system can be given as follows: If a system is regular it normally features some symmetries and conserved quantities, in our case e.g. the Hamiltonian conserves S_z (i.e. m in the mean field picture) and is also symmetric under the transformation $m \mapsto -m$ for $r = 0$. This leads to degeneracies, energy levels (as a function of some other parameter, e.g. q) cross. If we now turn on a disturbance (in our case $\propto rS_x$), the conservation

of S_z is broken, thus also m is not conserved any more. Formerly allowed level crossings are now avoided, see fig. 6.

This level repulsion changes the distribution of energy level spacings: In the unperturbed case, as level crossings are allowed, the distribution is peaked at zero and follows a Poisson distribution $P(s) = e^{-s}$. Now with level repulsion, small spacings are suppressed and the distribution of energy level spacings, as follows from random matrix theory, is best approximated by a Wigner distribution $P(s) = \pi/2\ s\ e^{-\pi s^2/4}$. [23]

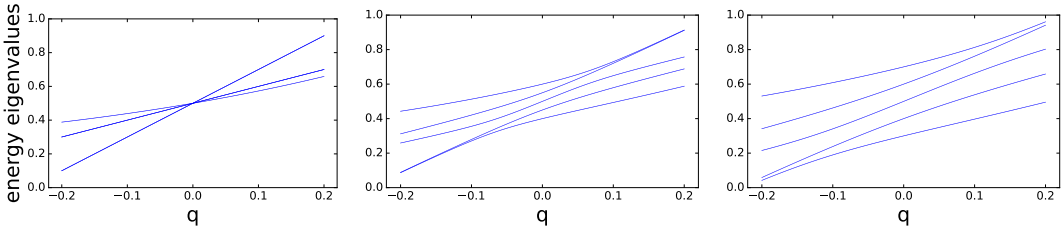

(a) $r = 0.00$ (b) $r = 0.05$ (c) $r = 0.1$

Figure 6: Detail of the eigenvalue spectrum as a function of the Zeeman parameter q for different values of r. For $r = 0$ the Hamiltonian exhibits symmetries, level crossings are allowed. For $r \neq 0$ these symmetries are broken, formerly allowed level crossings are now avoided. Spectra calculated for $N = 2$ atoms, $g = 1/N$, corresponding to $\tilde{g} = 1$ in the classical case. This is due to the different normalizations in the classical and quantum Hamiltonians, see note after eq. (21).

In our case, the Hamiltonian (even in the perturbed case) is still invariant under the "spin flip" symmetry $m \mapsto -m$ which can be equivalently expressed as the transformation $|N_1, N_0, N_{-1}\rangle \mapsto |N_{-1}, N_0, N_1\rangle$. So in order to see some interesting changes in the level statistics, we first have to write our Hamiltonian with respect to an eigenbasis of this transformation such that the Hamiltonian becomes block diagonal and then do the level spacing analysis in each block separately. A convenient eigenbasis representation b' (given the representation b of the Fock state basis B) is given by the elements $\frac{1}{\sqrt{2}}\left(|N_1, N_0, N_{-1}\rangle \pm |N_{-1}, N_0, N_1\rangle\right)$ having eigenvalues ± 1 respectively.

$$A \cdot b \equiv A \cdot \begin{pmatrix} |0,N,0\rangle \\ |0,N-1,1\rangle \\ |1,N-1,0\rangle \\ \vdots \\ |N_{-1},N_0,N_1\rangle \\ \vdots \\ |N,0,0\rangle \end{pmatrix} = \begin{pmatrix} |0,N,0\rangle \\ \frac{1}{\sqrt{2}}(|0,N-1,1\rangle + |1,N-1,0\rangle) \\ \\ \vdots \\ \\ \frac{1}{\sqrt{2}}(|0,N-1,1\rangle - |1,N-1,0\rangle) \\ \vdots \end{pmatrix} = b' \qquad (51)$$

Computationally, the basis transformation matrix A has been computed, then, after applying the transformation $H' = A\ H\ A^{\mathrm{T}}$, the eigenvalues for each block of the Hamiltonian have been individually calculated.

In a next step, the spectra are unfolded in the following way, described in [24]: Each spectrum is divided into several (in our case 10) regions. Then, in each region the level spacings are calculated as the difference between neighbouring eigenvalues and normalized (divided) by the mean level spacing in that region. This procedure ensures that the mean of all level spacings is equal to 1 and hence also that the (local) density of states is unity.

After this, the level spacings s are visualised in a single histogram where also the Poisson (green) and Wigner (red) distributions are plotted, see fig. 7. To get a quantitative estimate "how chaotic" the Hamiltonian is, the so-called Brody distribution $P_b(s)$ was fitted to the data (blue). This distribution interpolates between the Poisson ($b = 0$) and the Wigner distribution ($b = 1$) and is given by

$$P_b(s) = \alpha(b+1)s^b \exp\left[-\alpha s^{b+1}\right]\ ,\ \alpha = \left[\Gamma\left(\frac{b+2}{b+1}\right)\right]^{b+1} \qquad (52)$$

We see, that for $r = 0.00$ in fig. 7a the distribution almost perfectly follows a Poisson distribution. We expect this result as the classical theory is regular in the unperturbed case. Even though the distribution in fig. 7b is not perfectly described by the Wigner distribution, the Brody interpolation parameter $b \approx 0.6$ shows that the system is chaotic just as we expect from the classical theory. In fig. 7c we see, that for large disturbances r the Hamiltonian is again regular. As

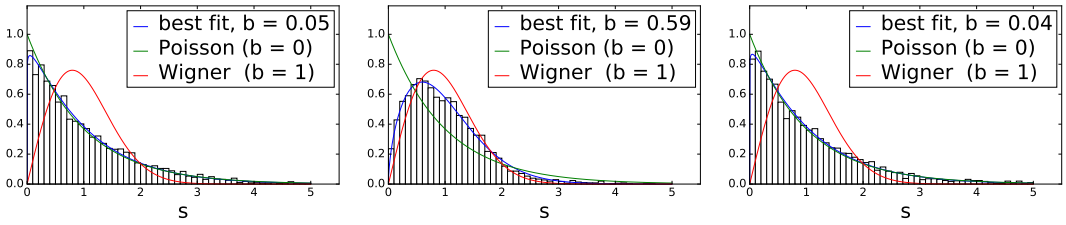

(a) $r = 0.0$ (b) $r = 0.5$ (c) $r = 1.85$

Figure 7: Histograms of the level spacing distributions for different disturbances r. Combined distributions of the subspaces defined by the spin flip symmetry, see text. $N = 100$ atoms (leading to 5091 energy eigenvalues) have been used to calculate these distributions with $g = 1/N$, $q = 1$.

already mentioned this is because in for large r the Hamiltonian is dominated by the S_x term and thus not chaotic any more.

All in all, we see that the level statistics of the Hamiltonian for as few as $N = 100$ atoms already nicely reflect the chaotic and regular parameter regions of the classical limit of the theory. But as we want to find a quantum mechanical quantity that implies that the classical theory is chaotic, the analysis of level spacings is not helpful: A quantum mechanical Hamiltonian with energy spacings following a Wigner distribution does not imply classically chaotic behaviour. Rather, both the Wigner distributed level spacings on one hand and classical chaos on the other hand are consequences of broken symmetries as parameters in the Hamiltonian are changed. Furthermore, the analysis of level statistics makes only global statements and hence does not allow to draw conclusions about the structure of regular and chaotic regions: E.g. a mixed phase space has no correspondence in terms of the level statistics. Nevertheless, the analysis of level spacings provides a necessary, though not sufficient condition for chaotic behaviour.

Finally, we note that experimentally it is very complicated to measure the whole energy spectrum of a Hamiltonian. That is why we turn to OTOCs at last, as they promise to be a quantity having a well-defined classical limit and are (not easily, but still) measurable experimentally.

4.5 OTOCs

As already mentioned in section 2.1, OTOCs have been introduced as a quantum measure corresponding to classical Lyapunov exponents. So if we want to construct a meaningful OTOC in the sense that we want it to correspond to a Lyapunov exponent in the classical limit, we have to consider the following:

An OTOC of the form $|[A(t), B]|^2$ includes the commutator $[A(t), B]$ thus corresponds to the (classical) Poisson bracket $\{A(t), B\}_{Poisson}$. The Poisson bracket is defined as

$$\{A, B\}_{Poisson} = \sum_{i=1}^{N} \left(\frac{\partial A}{\partial q_i} \frac{\partial B}{\partial p_i} - \frac{\partial A}{\partial p_i} \frac{\partial B}{\partial q_i} \right) \tag{53}$$

where (p_i, q_i) are pairs of canonical conjugate variables, i.e. they satisfy the Hamilton equations

$$\dot{p_i} = -\frac{\partial \mathcal{H}}{\partial q_i} \ , \qquad \dot{q_i} = \frac{\partial \mathcal{H}}{\partial p_i} \tag{54}$$

I.e. to be able to evaluate the Poisson bracket above, we first have to find canonical variables. It can be shown that in our case (ρ_0, Θ_s) and (m, Θ_m) are such canonical variables by using energy conservation and writing the time derivative of the energy functional in terms of the differentials of the phase space variables.

Having in mind that we want to choose OTOCs that can be (rather easily) implemented experimentally, we notice that ρ_0 and m can be easily measured and also have simple representations in terms of the dipole-quadrupole operators, whereas representing Θ_s and Θ_m in these operators is not so easy. Thus we see that the Poisson bracket takes the form of a Lyapunov exponent (i.e. the derivative of some quantity to some initial condition of (possibly) another quantity) if we take $B = S_z$ or $B = \rho_0$. Because then we have e.g.

$$\begin{aligned} \{A(t), S_z\}_{Poisson} &= \frac{\partial A(t)}{\partial \rho_0} \frac{\partial S_z}{\partial \Theta_s} - \frac{\partial A(t)}{\partial \Theta_s} \frac{\partial S_z}{\partial \rho_0} + \frac{\partial A(t)}{\partial m} \frac{\partial S_z}{\partial \Theta_m} - \frac{\partial A(t)}{\partial \Theta_m} \frac{\partial S_z}{\partial m} \\ &\propto \frac{\partial A(t)}{\partial \Theta_m} \end{aligned} \tag{55}$$

Note that only the last term survives as in the classical limit $S_z = m$. Similarly, we get

$$\{A(t), \rho_0\}_{Poisson} \propto \frac{\partial A(t)}{\partial \Theta_s} \ . \tag{56}$$

Here, $A(t)$ can be the time evolution of any operator. But again having in mind the experimental realization and the fact that Θ_s and Θ_m have no (simple) rep-

resentation in terms of the dipole quadruple operators, it is sensible to choose A as one of these latter, i.e. $A \in \{S_i, Q_{ij}, (i,j) \in \{x,y,z\}\}$.

For the quantum mechanical calculations, the time reversal to calculate OTOCs has been implemented as follows: As OTOCs generally take the form

$$\langle\psi_0| \left|[A(t), B(0)]\right|^2 |\psi_0\rangle \tag{57}$$

for two (hermitian) operators A and B, we have two possibilities to calculate them: One would be to expand the expression above and calculate each of the four resulting terms by evolving the states forward and backward in time by numerical integration as explained in section 4.1. Alternatively, we could numerically diagonalize the Hamiltonian and compute the matrix representation of the time evolution operator $U(t) \equiv e^{-iHt}$. Although the diagonalization takes in principle longer than the numerical integration, the second way of calculating OTOCs is much more efficient, as the diagonalization has to be performed only once for each time: Having the matrix representation of $U(t)$, we can directly calculate $A(t) = U^\dagger(t)AU(t)$. From here it is straight forward to calculate the commutator and its expectation value with respect to some initial state $|\psi_0\rangle$. Whereas, if we want to use numerical integration, we have to perform 14 different time evolutions (there are four time evolutions in each of the four terms of the expanded OTOC but two of them cancel).

To compute the representation of $U(t)$ we numerically calculate the eigenvectors and eigenvalues of the Hamiltonian matrix. Let $V = \left(\vec{\Phi}_1, \ldots, \vec{\Phi}_n\right)$ be the matrix containing the eigenvectors of H as columns and $\Lambda = diag(\lambda_1, \ldots, \lambda_n)$ the diagonal matrix containing the eigenvalues of H as diagonal elements. Then $H = V\Lambda V^{-1}$ and

$$U(t) = e^{-iHt} = Ve^{-i\Lambda t}V^{-1} = V\ diag\left(e^{-it\lambda_1}, \ldots, e^{-it\lambda_n}\right)V^{-1}\ . \tag{58}$$

With this method, we can compute the time evolution of OTOCs for 100 points in time for up to $N = 75$ atoms (corresponding to a $n = 2926$ dimensional Hilbert space). Technically, we could go to much higher numbers of atoms, but in that case calculations take a lot of time already because of the numerous multiplications of high dimensional matrices.

5 Results: Comparison between Classical and Quantum Chaos

5.1 Classical Poincaré map vs. Visualisation of Quantum Calculations

In this section we want to check whether the visualization of simulated quantum states via projections onto a grid of coherent states (section 4.3) produces a picture consistent with the notion of a point in classical phase space moving with time. In a first step, we want to see that the probability distribution gets more and more peaked with increasing number of particles as we expect that in the limit of $N \to \infty$ it should be described by a delta distribution. This can be understood as follows: The mean field approximation in section 3.1 corresponds to a first order expansion in $1/\hbar$ or the so-called "truncated Wigner approximation" [25]. I.e., in the classical limit $N \to \infty$, the quantum mechanical probability distribution should converge to a single point in classical phase space whose time evolution is governed by the mean field equation of motion. In my simulations on an ordinary computer I cannot go to very high particle numbers, but to get an idea, I compared the visualisation of some state for $N = 10, 30, 60$ particles, see fig. 8. As we can see, the distributions indeed get more and more peaked, just as

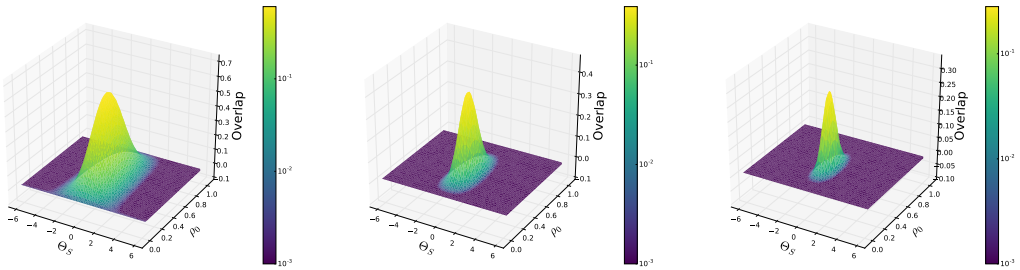

(a) $N = 10$ (b) $N = 30$ (c) $N = 60$

Figure 8: Projections onto a grid of coherent states for different numbers of particles N. The state that is shown is the coherent state classically corresponding to $\rho_0 = 0.4$, $m = 0.1$, $\Theta_s = 0 = \Theta_m$.

expected.

When plotting the probability distributions for a series of points in time,

one can clearly see that it disperses but also that it moves along one of the classical trajectories that can be seen e.g. in fig. 4a (for $r = 0$). If we increase the disturbance r such that we have a mixed phase space and start with an initial point near the border between a classically regular and classically chaotic region, we notice the following behaviour: At first, most of the distribution follows the classical trajectory but then, as the packet disperses until parts of it reach classically chaotic regions, it separates and stretches out until it eventually covers all of the energetically allowed phase space.

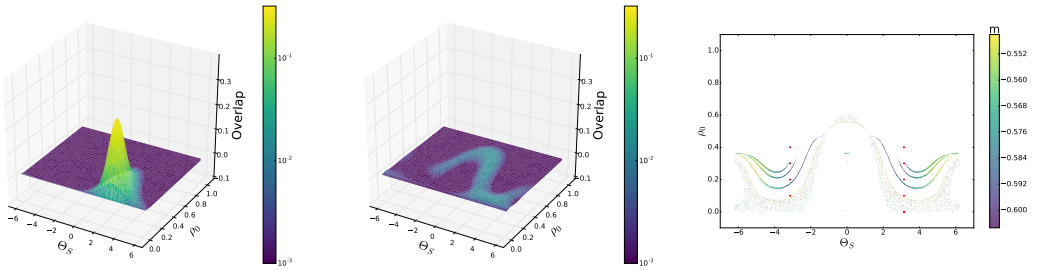

(a) $t = 0.3$ (b) $t = 8.0$ (c) Poincaré map

Figure 9: (a) and (b) Time evolution of projections onto a grid of coherent states at different times t for $r = 0.15$, $N = 60$, $g = 1/N$, $q = 1$. The initial state is the coherent state classically corresponding to $\rho_0 = 0.1$, $m = 0.1$, $\Theta_s = \pi$, $\Theta_m = 0$, thus lies close the border between a classically chaotic and a classically regular region of the phase space: (c) shows the Poincaré map for the classically corresponding parameters, $r = 0.15$, $\tilde{g} = q = 1$.

5.2 OTOCs vs. Classical Lyapunov Exponents

According to the derivation of OTOCs given in sections 2.1 and 4.5 their time evolution should correspond to that of (the square of) the derivative of some operator with respect to some initial value in the classical limit, i.e. $N \to \infty$. Here, we exemplify our observations with the help of the OTOC $\langle\psi_0| \left|[S_x(t), S_z]\right|^2 |\psi_0\rangle$. As already mentioned above, the simulations of OTOCs are computationally expensive such that we can only go to particles numbers $N \leq 75$ for reasonable times of the simulation. As we can never come close to the limit $N \to \infty$, we want to check how the functional form the time evolution of OTOCs changes with the number of particles: In fig. 10 we see that for small N there are larger

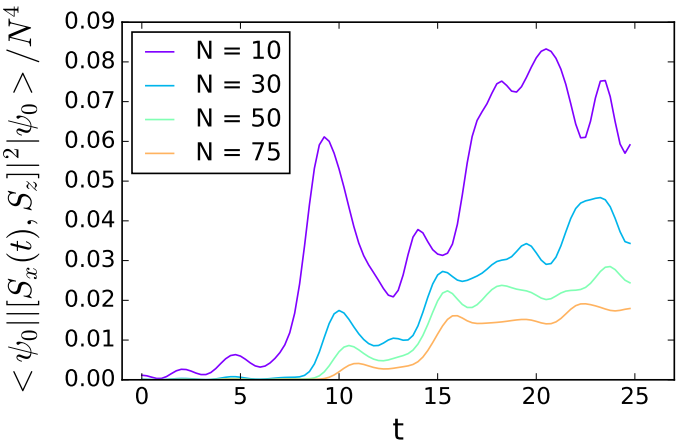

Figure 10: Comparison of the time evolution of the OTOC $\langle\psi_0| \, |[S_x(t), S_z]|^2 \, |\psi_0\rangle$ for different particle numbers N. The initial state $|\psi_0\rangle = |\psi_0^{(r)}\rangle$ is the coherent state corresponding to $\rho_0 = 0.2$, $\Theta_s = \pi$, $\Theta_m = 0$ and m calculated such that the total (mean field) energy is $E = 1.005$. The Hamilton parameters are $g = 1/N$, $q = 1$, $r = 0.15$ such that the settings correspond to those in fig. 5b with an initial state in the classically regular region.

fluctuations and for larger N the curves become smoother. We also note that for shorter times the functional form of the curves corresponding to $N = 50$ and $N = 75$ do not differ very much, indicating that even if we are far from $N \to \infty$, the functional form of the OTOCs should not deviate too much from that in the desired limit, at least for short times.

In a next step, we want to see qualitative differences for initial states and parameters that show regular and chaotic behaviour in the corresponding classical theory, respectively. For this purpose we pick two different initial states, one, denoted $|\psi_0^{(r)}\rangle$, lying in a classically regular and the other, denoted $|\psi_0^{(c)}\rangle$, in a classically chaotic region of phase space for $r = 0.15$, see e.g. figures 4b and 5b. If the OTOC reflects whether the system is regular or chaotic in the classical limit, there should be a significant difference between the time evolutions for $r = 0.0$, $r = 2.5$ and $r = 0.15$ for $|\psi_0^{(r)}\rangle$ on the one hand and $r = 0.15$ for $|\psi_0^{(c)}\rangle$ and both initial states with $r = 0.5$ on the other hand.

As we see in fig. 11 this is almost perfectly the case: In the classically regular cases, the OTOCs grow extremely slowly compared to the classically chaotic ones, except for the classically regular initial state for $r = 0.15$: We do not see a striking

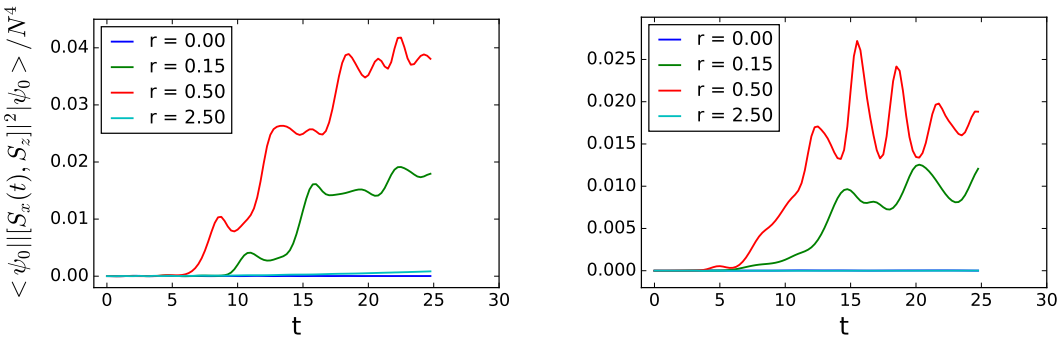

(a) initial state $|\psi_0^{(r)}\rangle$ (b) initial state $|\psi_0^{(c)}\rangle$

Figure 11: Functional form of the time evolution of the OTOC $\langle\psi_0| \left|[S_x(t), S_z]\right|^2 |\psi_0\rangle$ for different disturbances r. The OTOCs have been calculated for $N = 75$ atoms, $g = 1/N$, $q = 1$. In (a) the initial state $|\psi_0^{(r)}\rangle$ is the same as in fig. 10 and in (b) it is the coherent state $|\psi_0^{(c)}\rangle$ corresponding to $\rho_0 = 0.0$, $\Theta_s = \pi$, $\Theta_m = 0$ and m calculated again such that the total (mean field) energy is $E = 1.005$. Thus the main difference between the initial states is that for $r = 0.15$ the state in (a) corresponds to a classically regular state and the one in (b) to a classically chaotic one, see also fig. 12. Note, that this difference is only given for $r = 0.15$, for $r = 0.5$ they both correspond to classically chaotic initial states and for $r = 0.0$ and $r = 2.5$ both correspond to classically regular ones.

difference depending on the different initial states for $r = 0.15$ as we hoped. To investigate this further, we directly compare their time evolution in fig. 12.

In fig. 12 we indeed see a qualitative difference between the time evolutions of the OTOC with respect to the different initial states $|\psi_0^{(r)}\rangle$ and $|\psi_0^{(c)}\rangle$ although they look similar at first:

Both evolutions start at the same value, remain almost constant for some time and eventually saturate at later times showing oscillatory behaviour. This is partly what we expected: It is clear that OTOCs should start at a well defined value, in this case given by $\langle\psi_0| \left|[S_x, S_z]\right|^2 |\psi_0\rangle = \langle\psi_0| \left|S_y\right|^2 |\psi_0\rangle$ and it is also clear that they cannot grow indefinitely, i.e. they have to saturate at some point due to the finite Hilbert space.

The qualitative differences between the OTOCs corresponding to the different

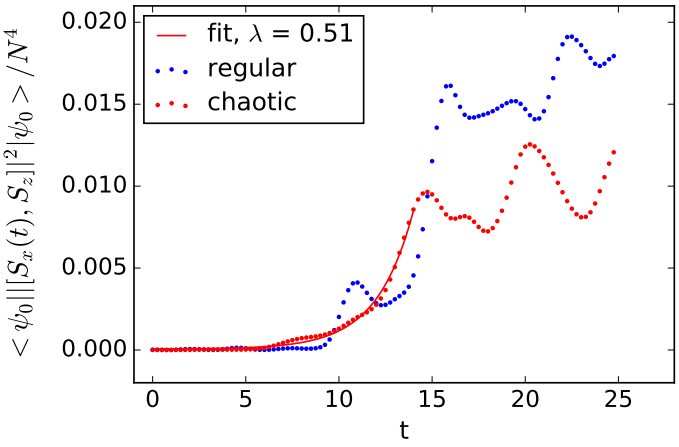

Figure 12: Comparison between the time evolution of the OTOC $\langle\psi_0| \left|[S_x(t), S_z]\right|^2 |\psi_0\rangle$ for different initial states: One corresponding to a state in a classically regular region (blue dotted line) and one corresponding to a classically chaotic one (red dotted line). The latter has been fitted using $f(x) = Ae^{\lambda x}$ (solid red line).The initial states are the same as in fig. 11. The OTOCs have been calculated for $N = 75$ atoms and $g = 1/N$, $q = 1$, $r = 0.15$ such that the settings correspond to those in fig. 5b.

initial states are visible between these two time-regimes: The OTOC corresponding to the classically chaotic initial state $|\psi_0^{(c)}\rangle$ grows monotonously while the other oscillates while growing. These oscillations could be a sign of regular behaviour as they could indicate that the state "comes back" to a similar state as before which hints at closed orbits in the corresponding classical phase space. The fact that also the OTOC with respect to $|\psi_0^{(r)}\rangle$ grows after some time and does not just oscillate around a low value could be explained as follows: The coherent initial state corresponds to a distribution of states in classical phase space with non-zero width. All included states evolve regularly but also independently from the others, i.e. the wave packet disperses along the classical trajectory which leads to the growth of the OTOC. Another reason could also be that the wave packet describing the coherent state disperses such that it overlaps with classically chaotic regions. This is possible because the initial state $|\psi_0^{(c)}\rangle$ lies close to a chaotic region in classical phase space. In this case we would also expect the OTOC to grow.

Also, almost certainly the semi-classical picture that we invoke here, breaks

down at late times. This is equivalent to the fact that semi-classical (phase space) methods like the truncated Wigner approximations are inherently short time methods, and at long times (for any finite particle number) quantum fluctuations become dominant. The challenge of finding meaningful OTOCs in the sense that they can be used as a proxy for classical chaos, will be to reach a regime where the expected semi-classical behaviour (exponential growth or regular, periodic dynamics) occurs before the semi-classical description breaks down.

Theoretically, by construction, OTOCs should grow exponentially up to some time if the corresponding classical Lyapunov exponent is larger than zero. It is indeed possible to fit an exponential function to the simulated data, see fig. 12. The exponent we obtain from the fit is of the same order as the exponent we get from fitting an exponential function to the numerically calculated derivative $\left|\frac{\partial S_x(t)}{\partial \Theta_{m,0}}\right|^2 \propto e^{2\lambda t}$, but it is approximately twice as large as expected. We would need much more simulation data to decide whether the exponential growth of the OTOC converges to (twice) the corresponding Lyapunov exponent. Another problem is, that for some OTOCs the exponent we get for a classically regular initial state is greater than the one corresponding to a classically chaotic one. It is not clear if this is due to the rather small particle numbers that we can simulate or if OTOCs truly fail in some cases to distinguish between classically regular and chaotic behaviour.

6 Summary

In this thesis the connections between quantum and classical chaos in a spinor Bose Einstein condensate have been investigated theoretically and numerically. In the first part, the corresponding classical theory has been derived and probed for classical chaos using well established concepts: Poincaré sections and Lyapunov exponents. Then, in the quantum theory, chaos has been investigated by analysing the level statistics of the Hamiltonian and finally OTOCs. Examples have been given for meaningful OTOCs in the theory of spinor BECs: Correlators that correspond to the derivative of a classical quantity with respect to the initial value of some phase space coordinate, i.e. those OTOCs that are characterized by some well defined Lyapunov exponent in the classical limit.

Some examples of these OTOCs have been analysed with respect to the question whether they can be used to decide if the classical limit of the quantum system is regular or chaotic. We found that there are qualitative differences between OTOCs in these two cases but we could not find a quantitative and definitive criterion for unambiguously deciding between a regular and a chaotic classical limit. Because our simulations are strongly limited regarding the number of simulated atoms, this does not mean that there is no such criterion. Larger simulations or experimental measurements could lead to further insights.

7 Outlook

This work is focused on the possibility to detect quantum chaos using OTOCs. But these special correlators have also other applications: It has been shown recently that certain OTOCs can be used to quantify entanglement [26]. It has also been shown that the (second) Rényi entropy after a quench can be related to OTOCs [27]. If one could gain a better understanding of how OTOCs are related to entanglement measures such as the entanglement entropy or the quantum Fisher information, one could maybe use OTOCs to experimentally measure these quantities that are normally not directly accessible. Being able to measure entropy and entanglement would open a way to further investigate how these quantities relate e.g. to the thermalisation of quantum mechanical systems and could lead to new insights regarding quantum information theory.

Furthermore, OTOCs in spinor BECs offer the chance to understand what scrambling means in a non-local system: In general, scrambling can be interpreted as the process of distributing the information contained in the initial state over the system's degrees of freedom [26]. For example in spin chains, where local operators can be defined, an initial impurity on one site will eventually spread out and involve more and more spins with increasing time. In such a system, OTOCs measure the support of a given operator, i.e. the amount of spins involved. It is clear that in our system, where we have *collective* spinor dynamics, we have to find an alternative notion of such a "support" if we want to probe the scrambling rate in the spinor BEC.

Another aspect that has not been discussed in this work is the experimental measurement of OTOCs. Although it has been explained how one can in principle measure them by tuning the Hamiltonian parameters such that one can realize the time reversal schemes needed, a complete measurement scheme has yet to be developed. Being able to experimentally measure OTOCs would not only be helpful with regard to the detection of entanglement but would also answer some open questions of this work: As it would allow us to measure OTOCs in a BEC of tens of thousands of atoms, it would bring us closer to the classical limit than any simulation.

References

[1] Jordan S Cotler, Dawei Ding, and Geoffrey R Penington. Out-of-time-order Operators and the Butterfly Effect. *arXiv*, 1704.02979(4), 2017.

[2] Efim B. Rozenbaum, Sriram Ganeshan, and Victor Galitski. Lyapunov Exponent and Out-of-Time-Ordered Correlator's Growth Rate in a Chaotic System. *Physical Review Letters*, 118(8):1–5, 2017.

[3] C S Gerving, T M Hoang, B J Land, M Anquez, C D Hamley, and M S Chapman. Non-equilibrium dynamics of an unstable quantum pendulum explored in a spin-1 Bose-Einstein condensate. *Nature Communications*, 3, 2012.

[4] Morris W Hirsch, Stephen Smale, and Robert L Devaney. *Differential Equations, Dynamical Systems, and an Introduction to Chaos*. 2004.

[5] A I Larkin and Yu N Ovchinnikov. Quasiclassical Method in the Theory of Superconductivity. *Soviet Physics JETP*, 1969.

[6] Norman Y. Yao, Fabian Grusdt, Brian Swingle, Mikhail D. Lukin, Dan M. Stamper-Kurn, Joel E. Moore, and Eugene A. Demler. Interferometric Approach to Probing Fast Scrambling. *arXiv*, 1607.01801:1–6, 2016.

[7] Norman Y. Yao and Brian Swingle. Seeing Scrambled Spins. *Physics*, 10(July), 2017.

[8] J Kronjäger, K Sengstock, and K Bongs. Chaotic dynamics in spinor Bose–Einstein condensates. *New Journal of Physics*, 10, 2008.

[9] Edward N. Lorenz. Predictability: Does the flap of a butterfly's wings in Brazil set off a tornado in Texas? *American Association for the Advancement of Science Annual Meeting Prog.*, 1972.

[10] Ray Bradbury. A sound of thunder. *A Sound of Thunder and Other Stories*, pages 203–215, 2005.

[11] Igor L Aleiner, Lara Faoro, and Lev B Ioffe. Microscopic model of quantum butterfly effect: Out-of-time-order correlators and traveling combustion waves. *Annals of Physics*, 375:378–406, 2016.

[12] M. S. Chapman, C. D. Hamley, C. S. Gerving, T. M. Hoang, and E. M. Bookjans. Spin-nematic squeezed vacuum in a quantum gas. *Nature Physics*, 8(4):305–308, 2012.

[13] M. S. Chapman, C. D. Hamley, C. S. Gerving, T. M. Hoang, and E. M. Bookjans. Spin-nematic squeezed vacuum in a quantum gas, supplementary information. *Nature Physics*, 8(4):305–308, 2012.

[14] Wenxian Zhang, Su Yi, and Li You. Mean field ground state of a spin-1 condensate in a magnetic field. *New Journal of Physics*, 5, 2003.

[15] Dan M. Stamper-Kurn and Masahito Ueda. Spinor Bose gases: Symmetries, magnetism, and quantum dynamics. *Reviews of Modern Physics*, 85(3):1191–1244, 2013.

[16] G. Edward Marti and Dan M. Stamper-Kurn. Spinor Bose-Einstein gases. *arXiv*, 1511.01575, 2015.

[17] Philipp Kunkel, Maximilian Prüfer, Helmut Strobel, Daniel Linnemann, Anika Frölian, Thomas Gasenzer, Martin Gärttner, and Markus K Oberthaler. Spatially distributed multipartite entanglement enables Einstein-Podolsky-Rosen steering of atomic clouds. *arXiv*, 1708.02407:1–27, 2017.

[18] Ivar Bendixson. Sur les courbes définies par des équations différentielles. *Acta Mathematica*, 1901.

[19] M. Henon. On the numerical computation of Poincaré maps. *Physica D: Nonlinear Phenomena*, 5(2-3):412–414, 1982.

[20] Alan Wolf, Jack B Swift, Harry L Swinney, and John A Vastano. Determining Lyapunov exponents from a time series. *Physica 16D*, 285(317):285–317, 1985.

[21] Thomas L. Curtright, David B. Fairlie, and Cosmas K. Zachos. A compact formula for rotations as spin matrix polynomials. *Symmetry, Integrability and Geometry: Methods and Applications (SIGMA)*, 10, 2014.

[22] Michael Cross. Chapter 29 Quantum Chaos. *www.cmp.caltech.edu/˜mcc/Chaos_Course/Lesson29/Quantum.pdf*, pages 1–8, 2000.

[23] Tobias Graß, Bruno Juliá-Díaz, Marek Kus, and Maciej Lewenstein. Quantum chaos in SU(3) models with trapped ions. *Physical Review Letters*, 111(9):1–5, 2013.

[24] Aviva Gubin and Lea F Santos. Quantum chaos: An introduction via chains of interacting spins 1/2. *arXiv*, 1106.5557:5, 2012.

[25] Anatoli Polkovnikov. Phase space representation of quantum dynamics. *arXiv*, 0905.3384:1–92, 2009.

[26] Martin Gärttner, Philipp Hauke, and Ana Maria Rey. Relating Out-of-Time-Order Correlations to Entanglement via Multiple-Quantum Coherences. *Physical Review Letters*, 120(4):1–16, 2018.

[27] Ruihua Fan, Pengfei Zhang, Huitao Shen, and Hui Zhai. Out-of-time-order correlation for many-body localization. *Science Bulletin*, 62(10):707–711, 2017.

Erklärung

Ich versichere, dass ich diese Arbeit selbstständig verfasst und keine anderen als die angegebenen Quellen und Hilfsmittel benutzt habe.

Heidelberg, den 17.07.2018, ...

(Unterschrift)